

AD-A186 627

20030127128

12

DTIC FILE COPY

Technical Report No. 3
Contract N 00014-84-K-0472; NR 650-025

**SPRAY DEPOSITION : A FUNDAMENTAL STUDY OF DROPLET
IMPINGEMENT, SPREADING AND CONSOLIDATION**

D. Apelian, A. Lawley, G. Gillen and P. Mathur.
Department of Materials Engineering
Drexel University
Philadelphia, PA 19104

1 September 1987

Annual Report for Period 1 July 1986 - 30 June 1987

Approved for public release; distribution unlimited. Reproduction in whole or in part is permitted for any purpose of the United States government.

Prepared for
OFFICE OF NAVAL RESEARCH
800 N. Quincy Street
Arlington VA 22217

DTIC
SELECTED
OCT 22 1987
S D
CH

87 10 13 021

TABLE OF CONTENTS

ABSTRACT	3
INTRODUCTION	4
OBJECTIVE AND SCOPE OF RESEARCH PROGRAM	5
PARTICULATE SPRAY DEPOSITION	6
FUNDAMENTALS OF THE PROCESS	6
(1) Droplet Velocity in Flight	7
(2) Droplet Temperature in Flight and Solidification	9
PROGRAM STATUS	12
(1) THEORETICAL STUDIES	13
1.1 Determination of the Average Heat Content of the Spray	15
1.2 Determination of the Deposition Rate	17
1.3 Determination of Heat Extraction Parameters	17
(2) RESULTS OF MODELING STUDIES	18
(3) EVALUATION AND DISCUSSION OF THE MODEL	20
3.1 Results of Temperature Measurements	21
3.2 Microstructural Analysis	21
3.3 Evolution of Microstructure	23
CONCLUSIONS	24
REFERENCES	25
NOMENCLATURE	28
TABLES	
FIGURES	



Accession For	
NTIS GRA&I	<input checked="" type="checkbox"/>
DTIC TAB	<input type="checkbox"/>
Unannounced	<input type="checkbox"/>
Justification	
By _____	
Distribution/	
Availability Codes	
Dist	Avail and/or Special
A-1	

ABSTRACT



Net or near net shape products can be manufactured by technologies involving solidification processing, metal forming, particulate processing, and droplet consolidation. One example of droplet consolidation is spray deposition in the Osprey™ mode. In this process, a stream of liquid metal is atomized by an inert gas to form a spray of molten droplets; these are accelerated towards a substrate where they impinge and consolidate. Mathematical models have been developed to describe droplet-gas interactions in flight and droplet behavior on impact with the substrate. The models predict droplet velocity and temperature as a function of flight distance, the extent of droplet solidification on arrival at the substrate, and temperature distribution in the consolidated material during deposition. Measured values of droplet velocity, the progress of droplet solidification, and attendant temperature profiles after consolidation on the substrate substantiate the integrity of the models. This approach demonstrates the utility of modeling studies in order to establish quantitative guidelines for optimization of the process in terms of the evolution of microstructure in droplet consolidation.



INTRODUCTION

The high technology materials processing and manufacturing industries are in a period of intense global competition. It is also a time of rapid growth and change in this sector of the U.S. economy. Manufacturing efficiency in these industries has traditionally been achieved via economy of scale but this is changing. The focus is now on flexible manufacturing in which a variety of processes are available that are easily adapted to changing product requirements, as well as being highly efficient with respect to both energy and materials. For the manufacturing sector of the U.S. economy to develop a competitive edge in the world market, the nation's manufacturing industry must be significantly improved through the adoption of new highly efficient manufacturing processes.

To be competitive, any process must be highly materials and energy efficient. Thus, an intrinsic requirement of a new processing technology is net or near-net-shape capability (1,2) in which the finished or nearly finished part is produced by the shortest route consistent with service and performance demands. The part must not only have the final shape needed, but it must also exhibit minimum property requirements when that shape is achieved. Major advantages inherent to a net or near-net-shape manufacturing approach are:

- Shorter production times
- Improved part performance
- Reduced energy consumption
- Conservation of critical materials
- Reduced scrap and handling costs
- Smaller inventories

There are several approaches to net shape manufacturing of metallic materials; these utilize the generic technologies of solidification processing (1,3,4) metal forming (1,2,4-6) particulate processing (1,2,4,5,7-9) and droplet consolidation (10-12). Major similarities and differences between these approaches are illustrated in Figure 1.

In the current program, attention is directed to droplet consolidation in which the material, in the form of a spray of liquid droplets, impinges on a substrate to produce a thick deposit. Examples of droplet consolidation are low pressure plasma deposition/spraying (12) and the Osprey™ spray forming process (10,11). In plasma deposition, the starting material is in the form of solid powder particles; upon injection into the hot plasma the particles melt, atomize, and finally impact and consolidate at the substrate, Figure 1. The Osprey™ spray forming process involves atomization of the alloy melt and impingement on the substrate with attendant consolidation, Figure 1. Spray deposition, spray forming, and spray casting are terms used to describe processes involving droplet consolidation.

OBJECTIVE AND SCOPE OF RESEARCH PROGRAM

The objective of the present study is to develop a fundamental understanding of microstructural evolution during spray deposition. The microstructure and density of the final product are determined by the condition of the droplets prior to impingement on the substrate, in terms of their size distribution, heat content and number density in the spray. Both theoretical and experimental studies have been carried out to quantify these parameters. Specifically, a theoretical model has been used to predict the velocity and temperature profiles of the droplets in flight, taking into account the undercooling and solidification of the droplets. Droplet number density in the spray (or deposition rate) and droplet size distributions have been measured experimentally as a function of radial distance from the spray axis.

With a knowledge of these parameters, the mechanisms of droplet consolidation and solidification of the deposit have been modeled, based on a heat transfer analysis across the material. The model predicts temperature history experienced at any location within the deposit during its build-up, and this information is used to quantify the local solidification times within the deposit, the rate of advance of solid-liquid interfaces and the variation of grain size across the thickness of the deposit. Experimental studies are in progress to confirm the integrity of the model; these involve the measurement of temperature profiles and the scale of microstructural features at different locations within the deposit. The steps leading to the evolution of the microstructure from the instant of droplet impingement is described based on knowledge of the process fundamentals.

PARTICULATE SPRAY DEPOSITION

The droplet consolidation process analyzed here is Osprey™ spray deposition. A schematic of the process is given in Figure 2. Briefly, the alloy charge is induction melted in a crucible located on top of the spray chamber. During melting, the chamber is purged with nitrogen gas and a slight over pressure of nitrogen gas is fed into the sealed crucible to prevent oxidation at the surface of the melt. The molten alloy exits through a refractory nozzle in the bottom of the crucible.

In the atomizing zone below the crucible the molten metal stream is broken up into a spray of small droplets by nitrogen gas, typically at a pressure in the range 0.7-1.0 MPa. The liquid droplets are cooled by the atomizing gas and accelerated to the substrate where they impinge and consolidate to form a thick net or near-net shape deposit largely devoid of porosity. An on-line sensor linked to a microprocessor monitors the spray and the deposit during deposition, and adjusts processing conditions accordingly.

A number of shapes can be deposited by maneuvering the substrate beneath the spray, Figure 3. For example, a solid cylindrical geometry can be produced by spraying onto a rotating disc substrate. By spraying onto a rotating mandrel, coatings can be applied, or a thin or thick walled tube can be fabricated. Deposition onto a large diameter drum or wheel allows strip or sheet to be produced in a semi-continuous fashion. The major advantage of the process is that a rapidly solidified, near-net shape product can be fabricated in a single operation directly from the melt at deposition rates in excess of 0.3 kg/s. Metallurgically, the product exhibits a fine equiaxed grain structure with essentially no macroscopic segregation of alloying elements. More detailed descriptions of the Osprey™ process are given elsewhere (10,11).

FUNDAMENTALS OF THE PROCESS

The deposition process per se is depicted schematically in Figure 4. Depending on size and hence cooling rate, the droplets can be completely liquid, partially liquid, or completely solidified when they impact the substrate. Thus, to optimize the integrity of the deposit (i.e. microstructure, absence of porosity) it is essential that the physical

condition of the droplets, prior to and immediately after impact upon the substrate, be known. Mathematical models are described which predict the velocity and temperature profiles of the droplets in flight, the progress of solidification, and droplet-substrate interactions.

(1) Droplet Velocity in Flight

The metal spray is comprised of droplets of differing diameter and the model considers a single droplet diameter at a given time in order to calculate velocity and temperature profiles along the droplet's flight trajectory. Similarly, this calculation is carried out for different droplet diameters. Individual droplets are treated as spheres and are assumed to follow a linear trajectory in flight. Each droplet will be accelerated to a point in flight where its velocity equals the instantaneous velocity of the atomizing gas, i.e. the relative velocity is zero. Beyond this flight distance, the droplet will travel faster than the gas and consequently it will be decelerated.

The velocity profile is determined from the momentum equation which relates the acceleration of a droplet to the velocity of the gas relative to the droplet. The total force (F) acting on a droplet in a one-dimensional continuum gas flow is given by (13):

$$F = m(dV/dt) = (C_D \rho_g V_r^2 A / 2) + mg \quad (1)$$

$$\text{droplet acceleration} = (dV_d/dt)$$

$$= \{3C_D \rho_g (V_g - V_d) |V_g - V_d| / 4dr_d\} + g \quad (2)$$

where: m is the mass of the droplet, V_d is the droplet velocity
 V_g is the gas velocity, $V_r = (V_g - V_d)$ is the relative velocity
 t is the flight time, ρ_g is the gas density
 ρ_d is the droplet density, A is the cross-sectional area of the droplet
 g is the acceleration due to gravity, C_D is the drag coefficient

C_D is given by (14):

$$C_D = 0.28 + [6/(Re)]^{1/2} + [21/Re] \quad (3)$$

and $Re = V_r d / \nu$ (4)

where ν is the kinematic viscosity of the atomizing gas. This equation is applicable over a wide range of Reynolds numbers (i.e. 0.1-4000) with only a small deviation ($\pm 7\%$) from the standard drag curve.

The flight trajectory of the droplet is divided into short segments over which equation (2) is assumed to be valid. There is no analytical solution to equation (2); it is solved numerically at nodes separating the segments of flight (15).

The predicted variation in droplet velocity with flight distance is shown in Figure 5 for Ni-20 w/o Cr droplets of 20 μm , 40 μm , 80 μm and 130 μm dia. Each droplet is accelerated from the point of atomization up to its peak velocity, which decreases with increasing droplet diameter. Peak velocity is attained at the flight distance at which the relative velocity V_r is zero. The smaller the droplet diameter, the smaller is the flight distance at which peak velocity is attained. At any given flight distance, there is a range of droplet velocities which correspond to the spread of droplet sizes. The predicted range of droplet velocities at three representative flight distances is shown in Figure 6.

To determine the average value of droplet velocity, the metal spray was examined by means of short exposure (0.00025s) still photography. The field of view of the camera covered droplet flight distances from 300 to 400mm. Measured velocities used in the comparison with the model are for a Ni-20 w/o Cr alloy.

The measured average velocity of droplets in the metal spray is greater than 100 m/s. Thus, the model predicts droplet velocities of the correct order of magnitude for droplet diameters below about 35 μm , Figures 5 and 6. The predicted velocities are lower than 100 m/s for larger droplet diameters. There are four limitations inherent in the photographic method that introduce error in measurement: (a) the plane of droplet trajectory is not necessarily parallel to that of the film, (b) the size of the droplet cannot be estimated from its corresponding streak on the film, (c) the droplet velocity is not constant over the streak length, and (d) the spray density is high and measured streak lengths may result from the overlapping of two or more individual streaks.

(2) Droplet Temperature in Flight and Solidification

To model the temperature history and solidification of droplets, the schematic profile shown in Figure 7 is adopted. For a given droplet, its initial temperature T_i is determined by the degree of melt superheat. The droplet cools by losing heat to the surrounding gas by convection and radiation until the nucleation temperature T_n is reached; this may be below the equilibrium liquidus temperature, as shown in Figure 7. The operative heat balance is:

$$Q_g = hS(T_d - T_g) + \sigma \epsilon S (T_d^4 - T_g^4) \quad (5)$$

where Q_g is the heat loss during flight, h is the convective heat transfer coefficient, S is the droplet surface area, σ is the Stefan-Boltzman constant, ϵ is the emissivity, and T is the temperature (the subscripts d and g refer to the droplet and gas, respectively). Heat loss from the droplet during flight can also be expressed as:

$$Q_g = mC_d \Delta T / \Delta t \quad (6)$$

where m is the mass of the droplet, C_d is the specific heat of the liquid, and ΔT is the change in droplet temperature over the time step Δt . The change in temperature ΔT over each time step Δt can be calculated by combining equations (5) and (6). From the instantaneous droplet velocity, ΔT can be measured over each segment of flight distance.

Heat transfer between the droplet and the surrounding gas is assumed to be interface controlled since the Biot number (hd/K_d) is < 0.1 . The convective heat transfer coefficient h is then given by (16):

$$h = K_g (2 + 0.6 Re^{0.5} Pr^{0.33}) (C_g^{Avg} / C_g)^{0.26} / d \quad (7)$$

where K_g is the thermal conductivity of the gas, Pr is the Prandtl number, C_g is the specific heat of the gas at temperature T_g , and C_g^{Avg} is the specific heat of the gas at an average temperature $(T_d + T_g)/2$. The specific heat ratio C_g^{Avg} / C_g is included to account for the higher local temperature of the gas immediately surrounding the droplet (17).

In order to predict the droplet temperature profiles, it is necessary to know to what extent undercooling occurs. Two extreme conditions are considered: no undercooling (i.e. heterogeneous nucleation) and complete undercooling (i.e. homogeneous nucleation). For homogeneous nucleation, the critical undercooling ΔT_c is given by (18):

$$(\Delta T_c / T_l)^2 = 16\pi\gamma^3 / 3\Delta H_f^2 kT \ln(N) \quad (8)$$

where T_l is the liquidus temperature of the alloy (Figure 7), ΔH_f is the latent heat of fusion, k is the Boltzman constant and N is the number of atoms in the droplet. In terms of Figure 7, $T_n = T_l$ if there is no undercooling, and $\Delta T_c = T_l - T_n$ for complete undercooling.

For the condition of no undercooling, projected temperature profiles for three droplet sizes are illustrated in Figure 8. It is observed that, with increasing droplet size, the onset and completion of solidification are delayed to larger flight distances. More importantly, as the droplet size increases, the flight distance over which solidification occurs also increases; this increases the likelihood of mushy impact at a given flight distance.

If any undercooling exists in the droplets, the effect of recalescence must be included in the model. Nucleation at T_n causes the temperature of the droplet to increase to T_a due to release of latent heat, Figure 7. Solidification is assumed to occur by the growth of thermal dendrites into the supercooled melt. The problem is to determine the recalescence arrest temperature (T_a) and the fraction of the droplet that has solidified during recalescence (f_s^r).

The rise in temperature during recalescence is divided into short increments of temperature rise ΔT , or increments of the fraction of the droplet that is solid, Δf_s . After each increment in temperature, the rate of heat release $Q_{r\theta}$ from the solidifying droplet is given by:

$$Q_{r\theta} = \Delta H_f V_{dg} v S \rho_d \quad (9)$$

where S is the surface area of the droplet. The dendrite growth velocity V_{dgV} is the only unknown in this equation, and is determined from the analysis of Langer and Muller-Krumbhaar (19):

$$p \exp(p E_i(p)) = \Omega \quad (10)$$

where p is the peclet number ($V_{dgV} r_{den}/2D$), E_i is an integral-exponential function, Ω is the thermal supersaturation $(T_l - T)/\Delta T_c$, r_{den} is the dendrite tip radius and D is the solute diffusion coefficient in the liquid.

V_{dgV} decreases as recalescence proceeds. Consequently, Q_{re} decreases during recalescence (equation 9). The limit in the increase of the droplet temperature (i.e. to the arrest temperature T_a) occurs when Q_{re} is equal to Q_g (as defined in equation 5).

After recalescence is complete, further solidification of the droplet is dictated by the Scheil equation (20). The final stage of cooling in Figure 7 occurs totally in the solid state.

For homogeneous nucleation, the predicted dependence of droplet temperature on flight distance is shown in Figure 9. Small droplets (40 μ m dia.) undercool and recalesce. Larger droplets (80 μ m and 130 μ m dia.) experience lower cooling rates and the extent of undercooling is insufficient to give rise to homogeneous nucleation, at least for flight distances <400 μ m. Under a condition of homogeneous nucleation, undercooling is sufficiently large that T_a is less than T_g , independent of droplet size. Thus, freezing is essentially instantaneous, and droplets are either completely liquid or completely solid at any selected flight distance.

From the calculated temperature profiles of droplets in the size range 20 μ m-150 μ m, it is possible to predict the largest droplet size d^* that will be solid at a given flight distance. The calculated dependence d^* on flight distance is given by Curve 2 in Figure 10 for the condition of homogeneous nucleation. For comparison, the corresponding relation between d^* and flight distance for a condition of no undercooling is included as Curve 1 in Figure 10.

The model for droplet temperature and solidification was assessed by comparison with experimental data and observations. Experiments were carried out on the Osprey™ facility at Drexel University. The alloy charge was induction melted under a nitrogen cover; nitrogen was also used as the atomizing gas (11,22). Deposition was carried out on flat refractory substrates positioned at various distances below the atomization zone (22).

To determine the extent of droplet solidification with flight distance, Ni-20 w/o Cr droplets in the spray were intercepted on glass slides at distances of 200mm, 275mm and 350mm from the point of atomization. The solidified droplets were examined by scanning electron microscopy.

A range of droplet sizes was observed on the glass slides. Small droplets were solid on impact with the slide and are spherical in shape with smooth surfaces. A fraction of the larger droplets was only partially solidified on impact with the glass collector plate and these fragmented via interdendritic regions. Droplets with larger amounts of liquid spread radially on the glass slide, and droplets that were completely liquid simply splatted on the glass collector plate.

The size of the largest solidified droplet (d^*) was determined at each of the three flight distances. Experimental data are included in Figure 10 which displays the model predictions for d^* under conditions of heterogeneous and homogeneous nucleation, i.e. curves 1 and 2, respectively. The measured values of d^* lie between these two curves. This confirms that the predicted extremes regarding undercooling are valid. The trend in the experimental data suggests that nucleation occurs under nearly homogeneous conditions in small droplets, Figure 10.

PROGRAM STATUS

The objective of the most recent phase of the research program has been to develop an understanding of microstructural evolution in spray deposited preforms. The commonly accepted model for microstructural development invokes a "liquid layer" on the surface of the deposit during its build-up (21), as shown schematically in Figure 4. As the

liquid in this layer solidifies due to heat removal through the substrate and the surrounding atomizing gas, additional liquid is added by incoming droplets and the net result is the presence of a liquid layer throughout the deposition process. Solidification of this type, wherein the solid evolves from a liquid layer on the deposit surface, is termed "incremental solidification" (21).

The presence of a liquid layer is of significance since it forms the initial state for solid formation. Direct experimental evidence of the liquid layer, its temperature and its thickness is extremely difficult to obtain. Similarly, it is difficult to determine the solidification profiles which govern the fineness of the final microstructure. In order to surmount this problem, our approach is to theoretically model the heat transfer/ thermal profile across a deposit during, and after, deposition. Quantitative results of temperature profiles within the deposit, thus obtained, are used to predict the solidification/cooling rates, motion of liquidus and solidus isotherms, fineness of microstructure and the level of porosity. The predictions of the model are subsequently verified experimentally.

(1) THEORETICAL MODEL

Microstructure across the deposit thickness is determined primarily by two competing parameters, namely deposition rate (\dot{D}) and the rate of solidification (\dot{S}). The effect of these two parameters is shown schematically in Figure 11. In Figure 11a, the solidification rate is greater than the deposition rate and a refined rapidly solidified microstructure is maintained throughout the deposit. If the deposition rate is greater than the rate of solidification a liquid (or partially liquid) layer can form and grow, see Figure 11b. This results in a coarse microstructure with increasing deposit thickness.

To model the thermal profile of the deposit during spray deposition, values of the following parameters must be known:

- (a) average heat content of the spray at the deposit surface (H_{spray})
- (b) deposition rate or increase in deposit thickness with time (\dot{D})
- (c) rate of heat removal by the substrate and the atomizing gas (h_s and q_c respectively)
- (d) metal properties

Factors (a) and (b) combine to yield the rate of heat input into the deposit, while (c) determines the rate at which heat is extracted from the deposit. Factor (d) governs the thermal gradients within the deposit. A one dimensional heat balance is established in the direction of deposit growth to yield the change in enthalpy with time at any position within the deposit. This formulation uses factors (a), (b), (c) and (d) and accounts for the moving boundary at the deposit surface such that:

$$\rho (\partial H/\partial t) = (1/L^2) \{ \partial/\partial \eta (K \partial T/\partial \eta) \} + (\rho \eta/L) (\partial H/\partial \eta) (dL/dt) \quad (11)$$

where:

L is the thickness of the deposit at any instant

$\eta = z/L$, z is distance into the deposit measured from the substrate upwards

H is the enthalpy at position z

$dL/dt = \dot{D}$ is the rate of deposit build up (deposition rate)

t is elapsed time from the start of deposition, ρ is the metal density and K is the thermal conductivity of the deposit.

Enthalpy, rather than temperature, is considered in Equation 11 to account for the two phase region during solidification. The boundary condition at the deposit - substrate interface ($\eta=0$) is:

$$(K/L) (dT/d\eta) = h_s (T_d - T_s) \quad (12)$$

where h_s is the heat transfer coefficient at this interface, T is the temperature and the subscripts d and s refer to the deposit and substrate, respectively.

The boundary condition at the top surface ($\eta=1$) is:

$$\rho (H_{\text{spray}} - H) (dL/dt) = K (dT/d\eta) + q_c \quad (13)$$

where q_c is convective heat loss by gas cooling, and

$\rho H_{\text{spray}} (dL/dt)$ is the heat flux input from incoming droplets.

Equation 11 is solved using a finite difference explicit numerical scheme at grid points positioned along the deposit thickness. While the total number of grid points is constant, the spacing between the points increases with the increase in deposit thickness

during deposition (uniformly expanding, time adaptive grid). Temperatures at each of the grid points at time $t+\Delta t$ are calculated from the temperatures available at these points for the previous time step, t . Therefore an initial estimate of the temperature profile along the deposit thickness is required at an infinitesimal time step after deposition begins. This information is provided by assuming a Newtonian heat transfer condition (i.e. no thermal gradients in the deposit) for the initial time step:

$$\rho L (dH/dt) = q_C + h_S (T_d - T_S) - \rho (H_{\text{spray}} - H) (dL/dt) \quad (14)$$

With a knowledge of the input parameters H_{spray} , D , h_S and q_C , and the material properties, thermal profiles existing at any location in the spray deposit can be predicted as a function of time.

1.1 Determination of the Average Heat Content of the Spray (H_{spray})

To determine the average heat content of the metal spray at the deposit surface, the following parameters must be quantified:

- (1) The radial distribution of droplet sizes in the spray at impact - determined from patternation studies.
- (2) The enthalpy (temperature and fraction solid) of individual droplet sizes at impact.

In the Osprey™ process, a stream of liquid metal, approximately 5mm in diameter, is atomized by high velocity gas jets arranged in a concentric circle around the metal stream. A spray cone of fine metal droplets is produced; this expands and increases in radius with increasing flight distance. The objective here is to determine the radial distribution of droplet sizes at a flight distance of 400mm where the spray is approximately 100mm in diameter. Atomization was carried out on Fe-20 w/o Mn alloy using a gas pressure of 8 bar (116 psi). Droplets were collected in copper tubes filled with water at three radial distances : along the central axis of the spray (0mm), and at distances of 26mm and 50mm from the spray axis. The set-up is shown schematically in Figure 12. The spray was allowed to continue for 5 seconds before it was cut off using a shutter mechanism.

Droplets collected in each of the three "rings" were filtered out, sprinkled onto

conducting tape and photographed on the SEM. These photographs were analyzed on an image analysis system to obtain a size distribution for each of the three radial distances. Typically, over a thousand particles were sampled from each ring. A population based distribution of droplet sizes was obtained, which was then converted to a distribution by weight by transforming the droplet diameter (d) to droplet volume (d^3). The above described experiment was carried out using different atomizing gasses. One set of runs was made with nitrogen as the atomizing gas, and another set whilst using argon atomization gas.

Representative droplet size distributions by population and weight are shown in Figure 13. The data are plotted from ring 3 using nitrogen as the atomizing gas. It is observed that the population distribution of droplet sizes is bi-modal, whereas the mass distribution is not. A bi-modal population distribution indicates that the spray comprises a very large fraction of fine droplets; these are solidified on impact and act as nuclei for solidification to produce the fine, equiaxed microstructure in the deposit. The variation of the mass-median droplet diameter with radial distance is shown in Figure 14 for argon and nitrogen. The following conclusions can be drawn from this figure: (i) Argon produces larger particle sizes compared to nitrogen. It is unclear if this is a consequence of a higher degree of powder agglomeration when argon was used. This possible phenomenon is currently being investigated. (ii) A sharper drop in droplet size with radial distance is observed with argon. The standard deviation in all cases was approximately 1.75.

A model to predict velocity and temperature profiles of individual droplets in flight was previously developed and is described in an earlier section. The model is run for droplet size distributions obtained from patternation studies for Fe-20 w/o Mn using different gas velocity profiles which vary from the center of the spray to its periphery (22). The degree of undercooling of these droplets was determined from glass slide experiments in the manner described previously. The fractional undercooling parameter f was found to decrease exponentially with increasing droplet volume, Figure 15. This quasi-empirical relationship between f and droplet volume is consistent with theoretical estimates of the probable number of nuclei per unit volume (23). Results from the model predict the condition of droplets, specifically their temperature and fraction solid, on impact at a flight distance of 400mm. Based on these calculations, the heat content of individual droplets on impact as a function of their size is predicted.

The average enthalpy of the spray at impact is determined by a statistical summation of the heat content of individual droplets:

$$H_{\text{spray}} = \frac{\sum H_p(d_i) d_i^3 f(d_i)}{\sum d_i^3 f(d_i)} \quad (15)$$

where $H_p(d_i)$ is the enthalpy for droplet of size d_i (from the model of droplet temperature) and $f(d_i)$ is the fraction of droplets with size d_i (from patterning studies, Figure 13). The heat content H_{spray} can be converted to an average temperature of the spray, T_{spray} , with a knowledge of the specific heat and the latent heat of fusion. T_{spray} is calculated to be 1358°C for Fe-20 w/o Mn at a flight distance of 400mm.

1.2 Determination of the Deposition Rate (\dot{D})

The spray density (# of droplets/unit area/unit time) is a maximum at the spray axis and decreases towards the periphery of the spray. Consequently, the rate of build up of the deposit is a strong function of distance from the spray axis. Theoretical predictions of the deposit build up rate are extremely difficult to make due to complexities in the atomization process and the effect of droplet splatting on impact.

Measurement of the build up rate \dot{D} is made using a video camera during deposition on a stationary substrate. An example of the thickness profile trace of Fe-20 w/o Mn deposit as a function of time is shown in Figure 16a. These profiles are then used to determine the average value of \dot{D} over the complete deposition cycle as a function of radial distance, as shown in Figure 16b.

1.3 Determination of Heat Extraction Parameters

The two heat extraction parameters are (1) h_s : the heat transfer coefficient at the deposit/substrate interface and (2) q_c : the convective heat loss by gas cooling.

(1) h_s : With cold, metallic (copper, steel) and non-metallic (alumina, cordierite, graphite) substrates, it is observed that the deposit usually adheres to the substrate for the first few

seconds but "lifts off" after some time. This occurs possibly due to contraction stresses upon solidification at the bottom of the deposit. "Lift off" produces an air gap between the substrate and deposit and changes heat transfer conditions during the deposition process. While no measurements of the heat transfer coefficient at the substrate have been carried out to date, it is necessary to measure h_s with a heat flux sensor embedded in the substrate. Such a sensor has been designed and is being fabricated.

(2) q_c : Cooling of the deposit by impact of a high velocity gas jet can be determined by assigning a heat transfer coefficient (h_g). Theoretical analysis and empirical data are available (24,25) wherein h_g is correlated with the velocity and thermal properties of the impinging gas jet. These correlations will be adopted once their applicability to the present conditions has been verified.

Since precise values of h_s and h_g are presently unavailable, a parametric study is in progress in which these parameters are varied over a wide range, namely $10^2 - 10^6$ $W/m^2/K$.

(2) RESULTS OF MODELING STUDIES

From equation (11), the dependence of the temperature distribution within the deposit is calculated as a function of time. Sample results are presented in Figure 17 for the spray deposition of Fe-20 w/o Mn. This particular alloy was chosen because, in conjunction with concurrent experiments on Fe-20 w/oCu, it provides a comparison of the effect of freezing range on the deposit microstructure. Both are iron based alloys with the same degree of alloying and nearly identical liquidus temperatures, $1450^\circ C$. However, Fe-20 w/o Mn has an equilibrium freezing range of $20^\circ C$ while the freezing range of Fe-20 w/o Cu is $350^\circ C$.

In Figure 17, \dot{D} was taken as $4mm/s$, and h_s and h_g were both 10^3 $W/m^2/K$. The calculated value of T_{spray} (from equation 15) was $1358^\circ C$; however the value of T_{spray} used to obtain the results in Figure 17 was taken to be $1395^\circ C$ based on experimental data from thermocouples within the deposit, as discussed in the following section.

Build up of the deposit takes about 40s, after which the thickness of the deposit remains constant, Figure 17a. From this figure it is possible to determine the thermal gradient across the thickness of the deposit at any instant of time, and also the variation in temperature distribution with time. The interval between the deposition line and the eutectic contour is a measure of the local solidification time t_f at any location within the deposit. It is observed that t_f increases rapidly over the initial thickness of the deposit, attains a maximum at the center, and then decreases due to gas cooling on the surface of the deposit.

Temperature distribution across the thickness of the deposit is transformed to the fraction of solid at these locations, assuming that solidification is governed by the Scheil equation (20). In this manner, the thickness of the liquid or partially liquid layer (containing $f_s < 1$) is determined at any instant of time; this is marked z_{pl} in Figure 17. The layer forms within a few seconds and grows on the surface of the deposit as deposition continues. Once deposition is completed, the layer thickness decreases from the top and bottom surfaces inwards due to heat extraction from these interfaces.

A plot of temperature against time elapsed from the start of deposition is given in Figure 17b. The curves represent the thermal history experienced within the deposit at three different heights (10mm, 40mm and 80mm) from the substrate, obtained from Figure 17a by drawing horizontal lines at these heights. At the 80mm location for example (i.e. the center of the deposit), it takes 20s for the deposit surface to build up to this height. Hence for the first 20s from the start of deposition, the temperature at this location remains at about 200°C. When the surface of the deposit reaches this location, the temperature increases almost instantaneously to the maximum temperature, 1380°C. Subsequently the temperature decreases and solidification is completed when the eutectic temperature T_e is reached. The local solidification time at this height, marked t_f in the figure, is about 300s.

The corresponding prediction of the model at a lower deposition rate of 3mm/s is shown in Figure 18. From a comparison of Figures 17 and 18, it is observed that higher deposition rates result in larger values of t_f and z_{pl} , implying that the resulting microstructure will be coarser. Local solidification times experienced at locations within the deposit are plotted for three representative deposition rates in Figure 19a. Under the conditions examined, the maximum in t_f , or the slowest solidification, occurs near the

center of the deposit. The variation of the thickness of the partially liquid layer z_{pl} is shown in Figure 19b at three deposition rates. For a given value of \dot{D} , z_{pl} increases to a maximum at the end of deposition (40s) and then decreases.

There is an initial thickness of the deposit, z_i , which forms before the development of a partially solidified layer. This region freezes almost instantaneously; however the rapidly solidified microstructure is generally accompanied by a high level of porosity. z_i is predicted to decrease with increasing values of \dot{D} .

(3) EVALUATION AND DISCUSSION OF THE MODEL

The results of the model were compared with experimental data and observations. Experiments were carried out on the Osprey™ spray forming facility at Drexel University. About 14 kg charge of Fe-20 w/o Mn was induction melted under a nitrogen cover; nitrogen was also used as the atomizing gas at a pressure of 8 bar (116 psi). Deposition was carried out on flat refractory substrates positioned approximately 400mm below the point of atomization. In order to measure the temperature within the spray deposits, thermocouples were initially set at specific heights above the stationary substrate surface at a radial distance of 10mm from the spray axis. Type 'B' (Pt.6%Rh-Pt.30%Rh) thermocouples were used and the bead (~1mm dia.) was exposed in order to achieve minimal response times. Data from the thermocouples were recorded on a 12-bit data acquisition system at intervals of about 30ms. A two color optical pyrometer was used to monitor the temperature of the top surface of the deposit.

The deposits were sectioned for microstructural analysis, polished, and dip etched in 10% nital. The variation in solidification cell size and porosity with thickness and radial distance from the spray axis was measured on a Zeiss image analysis system. Optical and scanning electron microscopy was conducted to study the microstructure of the deposits, overspray powders and powders collected in water from the patterning experiments. Identification of phases within the deposit and overspray powders was performed by X-ray diffraction and by WDX microprobe on the SEM. Differential thermal analysis (DTA) was carried out on the charge material, on samples from the deposit, and on overspray powders using a DuPont 1090 system.

3.1 Results of Temperature Measurements

The temperature profile recorded by one of the four thermocouples set within the deposit is displayed in Figure 20. The initial rise in temperature (at $t=0$) results from the start of the metal spray; droplets incident on the thermocouple tip consolidate to form a "bulb" around the exposed bead. At $t=5s$, the surface of the deposit reaches the thermocouple and a corresponding increase in temperature is observed. Due to bulb formation, the response time of the thermocouple is increased, and it takes a few seconds before the measured temperature reaches the actual temperature of the top surface. The local solidification time t_f is measured as the interval between the second rise in temperature and the time at which the temperature decreases to the eutectic temperature, T_e .

Temperature profiles thus obtained provide a direct comparison with the predictions of the model, as in Figure 17b. The maximum temperature (T_{max}) recorded by the thermocouples (at the "plateau" in the thermal profiles) was $1380^{\circ}C$. Therefore, T_{spray} should be greater than $1380^{\circ}C$, and also significantly higher than the calculated value of $1358^{\circ}C$ from equation (15). This discrepancy in T_{max} cannot be resolved at present; it can arise from errors in the measurement of the droplet size distribution or the prediction of the droplet enthalpy at impact. In the latter case, the errors are amplified for Fe-20 w/o Mn since the freezing range is narrow and small changes in temperature are accompanied by significant changes in the heat content. Therefore, T_{spray} is taken to be $1395^{\circ}C$ in the model so that the predicted maximum temperature is comparable with experimental measurements. With this correction, the predicted temperature profiles show good agreement with the experimental data, as shown in Figure 20.

3.2 Microstructural Analysis

Representative micrographs of a deposit produced on a stationary substrate are shown in Figure 21. The initial zone at the bottom surface has a fine martensitic structure consistent with rapid quenching by the substrate, Figure 21a. There is also evidence of prior particle boundaries that arise from insufficient welding between the liquid and presolidified droplets arriving at the substrate. Presolidified droplets result in a high level

of porosity (~14%) in the deposit; the pores are irregularly shaped and are generally interconnected. The thickness of this porous zone is of the same order of magnitude as the thickness of the deposit z_i which forms before the development of the partially liquid layer. In this region ($z < z_i$), the alloy freezes rapidly ($\dot{S} > \dot{D}$), and there is insufficient time for the liquid to flow and fill the space between presolidified droplets. Therefore the lack of a partially liquid layer is associated with porosity and poor microstructural homogeneity within the deposit. With increasing radial distance from the spray axis, the deposition rate decreases and both, z_i (predicted from the model) and the thickness of the porous zone (measured from the deposit), increase as shown in Figure 22.

At locations above the initial porous zone z_i , the microstructure is homogeneous and comprises individual grains with no prior particle boundaries (Figure 21b). The microstructure comprises hcp Fe-Mn martensite/Widmanstätten plates as confirmed by x-ray diffraction. This structure is similar to ingot cast Fe-20 w/o Mn alloys. The austenitic start and finish temperatures, determined by DTA, are also comparable with data in earlier reports (24,25). When the optical image is defocused, the solidification cell size becomes discernible (Figure 21c); it was found to increase with deposit thickness, attain a maximum and then decrease towards the top of the deposit, as in Table I. This trend is consistent with the variation in t_f predicted from the model (Figure 19a).

The computed values of local solidification time were used to predict cell sizes in the deposits based on empirical relationships for ingot cast Fe-20 w/o Mn (26):

$$CS = 150 (\Delta T_f / t_f)^{-0.5} \quad (16)$$

where CS is the predicted cell size (in μm) and ΔT_f is the freezing range of the alloy. The experimentally measured and the computed (from equation 16) values of the cell size are compared in Table I. Clearly, the measured values are significantly smaller than the cell sizes predicted by assuming normal solidification (equation 16). This implies that the nucleation density (N_v) in spray deposits is greater than the nucleation density during normal solidification. Therefore, prediction of the cell sizes within the deposit requires a knowledge of both, the nucleation density and the solidification rate or t_f . It is difficult to determine N_v because grain nucleation can occur at two types of nucleating sites:

- (a) at solid particles from the spray, the number density of which can be estimated from the droplet size distribution and the model for droplet temperature profile in

flight

- (b) at the large number of fragmented dendrite arms generated by the impact of a mushy droplet. This is observed by microscopic examination of the top surface of the deposit as shown in Figure 23. It is difficult to determine the number density of such nucleation sites.

The density of the deposit is typically greater than 99% of theoretical density (Figure 24a); the variation of the level of porosity at different radial distances from the spray axis (or values of \dot{D}) is shown in Figure 24b. Porosity which is present at locations higher than z_i is found to be isolated and nearly spherical. This porosity can arise from solidification shrinkage, gas entrapment, insufficient liquid feeding or a combination of two or more of the above.

At the periphery of the deposit where the deposition rate is always smaller than the heat extraction rate, a high degree of porosity is maintained throughout the thickness as shown in Figure 24b at $R=43\text{mm}$. This is because the liquid or partially liquid layer does not develop during the entire period of deposition, i.e. $z_i = L$, where L is the deposit thickness at a given radial distance ($R=43\text{mm}$) from the spray axis.

3.3 Evolution of Microstructure

Based on the results of the theoretical and experimental studies described above, it is possible to describe the development of microstructure during spray deposition via the Osprey™ process. Except in the initial porous zone where $\dot{S} > \dot{D}$, the deposit undergoes a process of droplet remelting, grain nucleation and growth followed by solid state coarsening. The proposed sequence leading to the final microstructure of the deposit is summarized in Table II and is depicted schematically in Figure 25.

CONCLUSIONS

1. The population-based distribution of droplet sizes in the metal spray was found to be bi-modal whereas the mass-based size distribution is gaussian, on a log-normal plot.
2. It is possible to model droplets in flight in the Osprey™ spray forming process to predict the dependence of velocity on flight time. Measured values of droplet velocity are of the correct order of magnitude for droplet diameters below about 35 μ m.
3. The temperature profile of droplets in flight has been modeled. Assessment of the model is made in terms of the largest solidified droplet size (d^*) as a function of flight distance; measured values of d^* indicate that the degree of undercooling f decreases exponentially with increasing droplet diameter.
4. With a knowledge of the heat content of individual droplets at impact, the deposition rate and the heat extraction parameters, heat transfer across the spray deposit has been modeled in order to predict thermal profiles. Deposit temperatures measured as a function of time are in close agreement with the model.
5. A partially liquid layer forms on the surface of the deposit during deposition; it grows rapidly until a majority of the deposit is mushy (solid+liquid). The local solidification time predicted by the model is in good agreement with the variation in microstructural features such as grain size and the level of porosity. The predicted grain sizes are significantly greater than those measured experimentally; this suggests that the solidification process in spray deposits is different from normal solidification.
6. The model predictions provide a base to describe the evolution of microstructure in spray deposits.

REFERENCES

1. Wright, P.W., "Near-Net Shaping - The Key to New Material's Exploitation", Materials and Design, Vol. 8, No. 3, May/June 1987, pp. 142-146.
2. "Net Shape Technology in Aerospace Structures", Volumes I through IV, National Academy Press, Washington, D.C., 1986.
3. Apelian, D., "Solidification Processing Advances", Innovations in Materials Processing, Bruggeman, G.A., and Weiss, V., eds., Plenum Press, New York, NY, 1983, pp. 247-272.
4. Welch, M.M., "Near Net Shape Case Histories", Precision Metal, Vol. 44, No. 3, March 1986, pp. 21-32.
5. Irving, R.R., "Near Net Shapes: Closing in on Materials Waste", Iron Age, Vol. 227, No. 21, 1984, pp. 31-40.
6. Chou, P.C., Carlzone, J. and Mueller, M., "Numerically Controlled Orbital Forging: Feasibility of High Precision", Proceedings of the Second International Conference on Rotary Metalworking Processes, IFS Publications Ltd., U.K., 1982, pp. 101-112.
7. Lawley, A., "Net Shape Manufacturing - The Utility of Powder Metallurgy Processing", Advanced Manufacturing Processes, Vol. 1, Nos. 3/4, 1986, pp. 517-530.
8. Kuhn, H.A., Ferguson, B.L. and Smith, O.D., "Pseudo Hot-Isostatic Pressing Using Conventional Presses", Metal Powder Report, Vol. 38, No. 6, 1983, pp. 321-323.
9. Kuhn, H.A., and Ferguson, B.L., "An Expert Systems Approach to Preform Design for Powder Forging", Metal Powder Report, Vol. 40, No. 2, 1985 pp. 93-95.
10. Leatham, A.G., Brooks, R.G. and Yaman, M., "The Osprey Process for the Production of Spray-Deposited Roll, Disc, Tube and Billet Preforms", Modern

Developments in Powder Metallurgy, eds., Aqua, E.N., and Whitman, C.I., Metal Powder Industries Federation, Princeton, N.J., Vol. 15, 1985, pp. 157-173.

11. Gilien, A.G., Mathur, P.C., Apelian, D. and Lawley, A., "Spray Deposition: The Interaction of Material and Process Parameters", Progress in Powder Metallurgy, eds., Carlson, E.A., and Gaines, G., Metal Powder Industries Federation, Princeton, N.J., Vol. 42, 1986, pp. 753-773.
12. Jackson, M.R., Rairden, J.R., Smith, J.S., and Smith, R.W., "Production of Metallurgical Structures by Rapid Solidification Plasma Deposition", Journal of Metals, Vol. 33, No. 11, 1981, pp. 23-27.
13. Ranger, A.A. and Nicholls, J.A., "Aerodynamic Shattering of Liquid Drops", AIAA Journal, Vol. 7, 1969, pp. 285-290.
14. Clift, R., Grace, J.R., and Weber, M.E., Bubbles, Drops and Particles, Academic Press, N.Y., 1978.
15. Dahlquist, G., Bjorck, A., and Anderson, N., Numerical Methods, Prentice Hall, N.J., 1974.
16. Ranz, W.E. and Marshall, W.R., "Evaporation from Drops, Part II", Chemical Engineering Progress, Vol. 48, 1952, pp. 173-180.
17. Kimura, I. and Kanzawa, A., "Experiments on Heat Transfer to Wires in a Partially Ionized Argon Plasma", AIAA Journal, Vol. 3, 1965, pp. 476-481.
18. Haasen, P., Physical Metallurgy, Cambridge University Press, U.K., 1978.
19. Langer, J.S. and Muller-Krumbhaar, H., "Theory of Dendritic Growth - I. Elements of a Stability Analysis", Acta Met, Vol. 26, No. 11, 1978, pp. 1681-1688.
20. Flemings, M.C., Solidification Processing, McGraw Hill, N.Y., 1974.
21. Singer, A.R.E. and Evans, R.W., "Incremental Solidification and Forming", Metals

Technology, Vol. 10, 1983, pp. 61-68.

22. Connelly, S., Coombs, J.S. and Medwell, J.O., "Flow Characteristics of Metal Particles in Atomized Sprays", Metal Powder Report, Vol.41, No. 9, pp. 653-661.
23. Boettinger, W.J. and Perepezco, J. H., "Fundamentals of Rapid Solidification", "Rapidly Solidified Crystalline Alloys", eds. Das, S.K., Kear, B.H and Adam, C.M, The Metallurgical Society, Warrendale PA, 1985, pp. 21-58
24. Tomota, Y., Strum, M. and Morris, J.W., "Microstructural Dependence of Fe-High Mn Tensile Behavior", Met. Trans, Vol. 17A, March 1986, pp.537-547
25. Tomota, Y., Strum, M. and Morris, J.W., "The Relationship between Toughness and Microstructure in Fe-High Mn Binary Alloys", Met. Trans, Vol. 18A, June 1987, pp. 1073-1081
26. Jones, H.; "Some Principles of Solidification at High Cooling Rates", Rapid Solidification Processing : Principles and Technologies, eds. Mehrabian, R, et. al., Claitor's Publishers, Baton Rouge LA, 1978, pp. 28-45

NOMENCLATURE

A	droplet cross sectional area
C_D	drag coefficient
C	specific heat
CS	solidification cell size
d	droplet diameter
d^*	largest solidified droplet
D	solute diffusion coefficient
\dot{D}	deposition rate
E_i	integral-exponential function
$f(d_i)$	fraction of droplets of diameter d_i
f_s	fraction solid
f_s^r	fraction solid during recalescence
f	fraction of homogeneous nucleation
F	force
g	acceleration due to gravity
h	heat transfer coefficient
H	enthalpy
ΔH_f	latent heat of fusion
k	Boltzman constant
K	thermal conductivity
L	deposit thickness
m	mass of droplet
N	number of atoms
N_v	nucleation density
p	pecllet number = $V_{dg} r_d / 2 D$
Pr	Prandtl number
q_c	convective heat flux
Q	rate of heat extraction
r	radius
R	radial distance from spray axis
Re	Reynolds number
S	droplet surface area

\dot{S}	solidification rate
t	time
T	temperature
ΔT_c	undercooling for homogeneous nucleation
ΔT_f	freezing range of alloy
V	velocity
z	growth axis, thickness
ϵ	emissivity
γ	surface energy
η	dimensionless thickness = z/L
Ω	thermal supersaturation = $(T_l - T) / \Delta T_c$
ρ	density
σ	Stefan-Boltziman constant
v	kinematic viscosity of gas

Subscripts

a	arrest
c	convective
d	droplet
den	dendrite
dgv	dendrite growth
e	eutectic
f	freezing
g	gas
i	initial
l	liquidus
n	nucleation
P	particle
pl	partially liquid
r	relative
re	recalescence
s	substrate

TABLE I

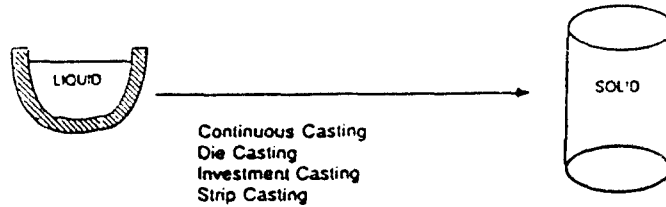
COMPARISON BETWEEN PREDICTED
AND MEASURED CELL SIZES

z (mm)	t_f (sec)	Predicted Cell Size (μm) (Equation 16)	Measured Cell Size (μm)
20	50	115	40
40	110	140	57
80	270	175	79
140	20	91	13

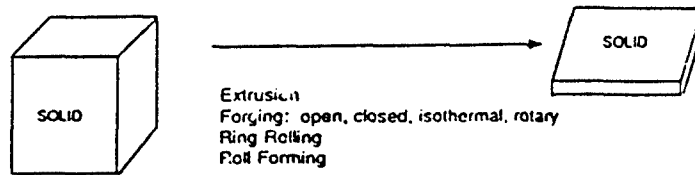
TABLE II

MICROSTRUCTURAL EVOLUTION	EVIDENCE
Input to deposit = solid, partially solid and liquid droplets of different f_s and temperature	<i>Spray simulation model, glass slide experiments and patterning</i>
Droplets land onto hot, partially liquid surface of the deposit (with $f_s > 0.6$)	<i>Model of deposit heat transfer and optical pyrometer recordings</i>
Solid droplets ($< d^*$) retain shape and size on impact, partially frozen droplets shatter interdendritically and liquid droplet splat	<i>Observation from glass slide experiments and morphology of deposit top surface</i>
Liquid wets solid particles. Localized heat flow from liquid to solid particles, leading to : (a) Interdendritic remelting (b) Solid remelting Remelting of solid continues until local temperature equilibrium is achieved. Remaining solid particles become nuclei for grain growth.	<i>No prior particle boundaries in bulk of deposit</i> <i>Difference between powder and deposit microstructure</i>
Growth of nuclei with attendant drop in local temperature, until T_0 is reached (end of t_f)	
Fine grain size due to high nucleation density from droplets remaining after remelting stage Large t_f or low solidification rate	<i>High density of broken dendrites on deposit surface + bimodal size distribution</i> <i>Predicted vs. measured cell sizes</i> <i>Theoretical and experimental values</i>
Solid state coarsening of the solidification structure	<i>Extensive coarsening in pure metals vs. limited coarsening in alloys with grain boundary precipitates</i>
No partially liquid layer initially. Grows rapidly during deposition until <u>majority</u> of the deposit is mushy (S+L)	<i>Structure changes rapidly in initial stages while layer forms, and then remains nearly constant due to large t_f</i>
Porosity is related to the formation of the partially liquid layer, i.e. to \dot{D}	<i>Thickness of initial porous layer vs. \dot{D}</i>

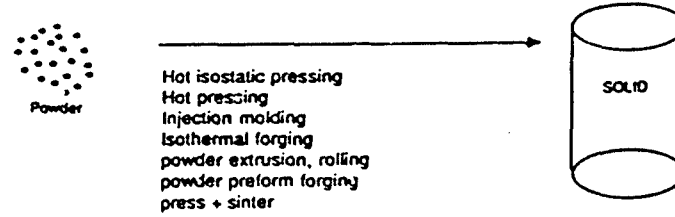
• SOLIDIFICATION PROCESSING



• METAL FORMING



• PARTICULATE PROCESSING



• DROPLET CONSOLIDATION

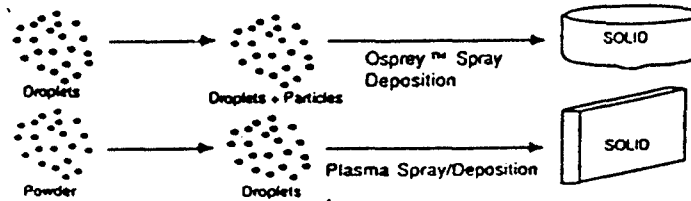


Fig. 1 Comparison of processing technologies for net or near net shape manufacturing

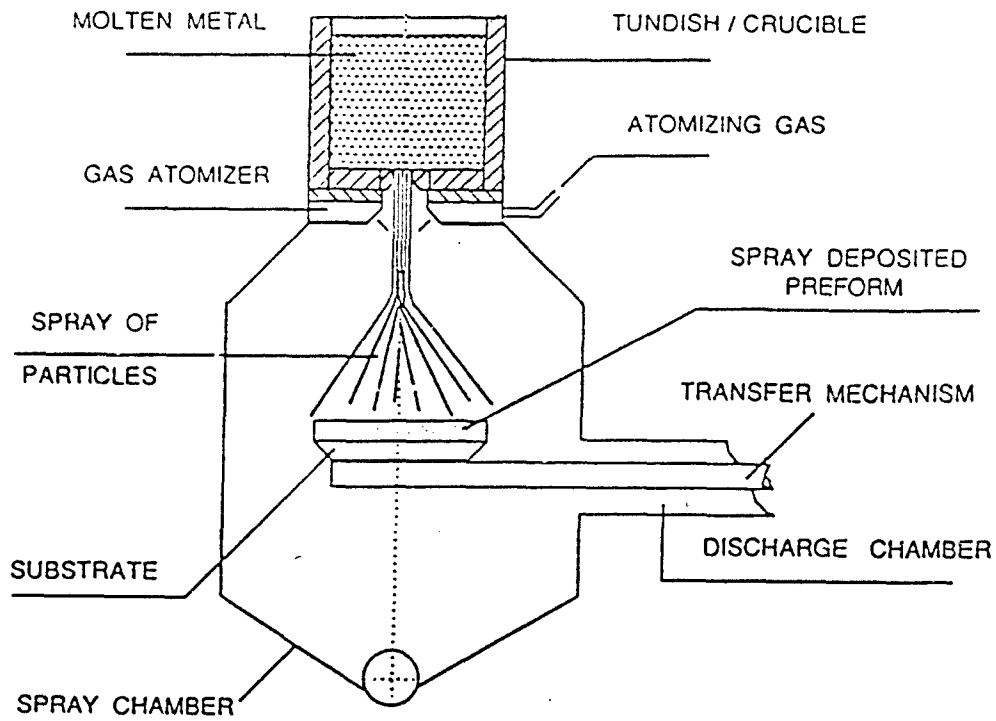


Fig. 2 Schematic of the Osprey™ process

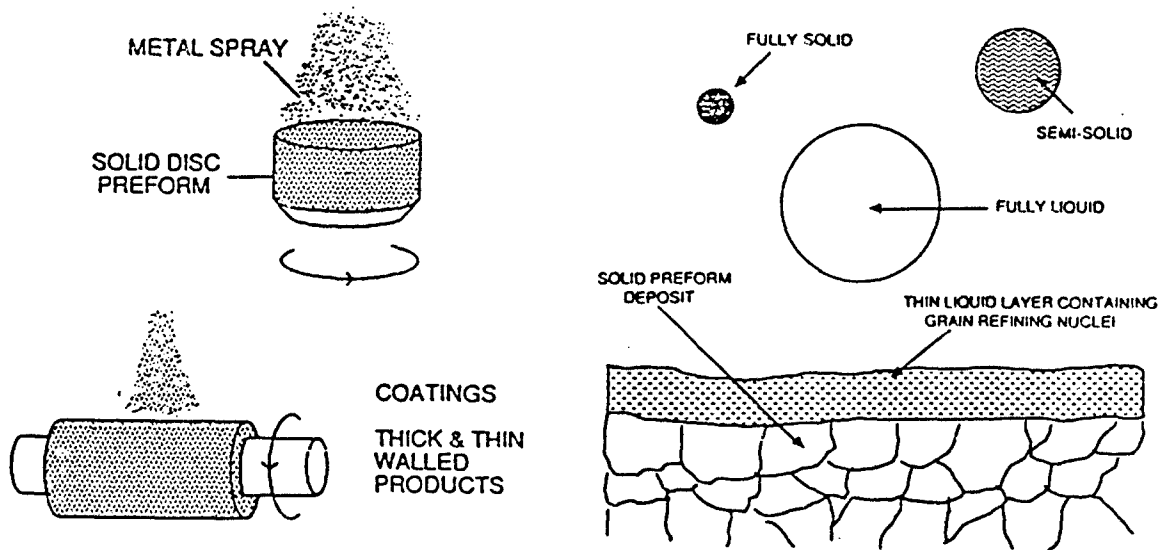


Fig. 3 Geometry of Osprey™ spray deposited shapes

Fig. 4 Schematic of droplet deposition process

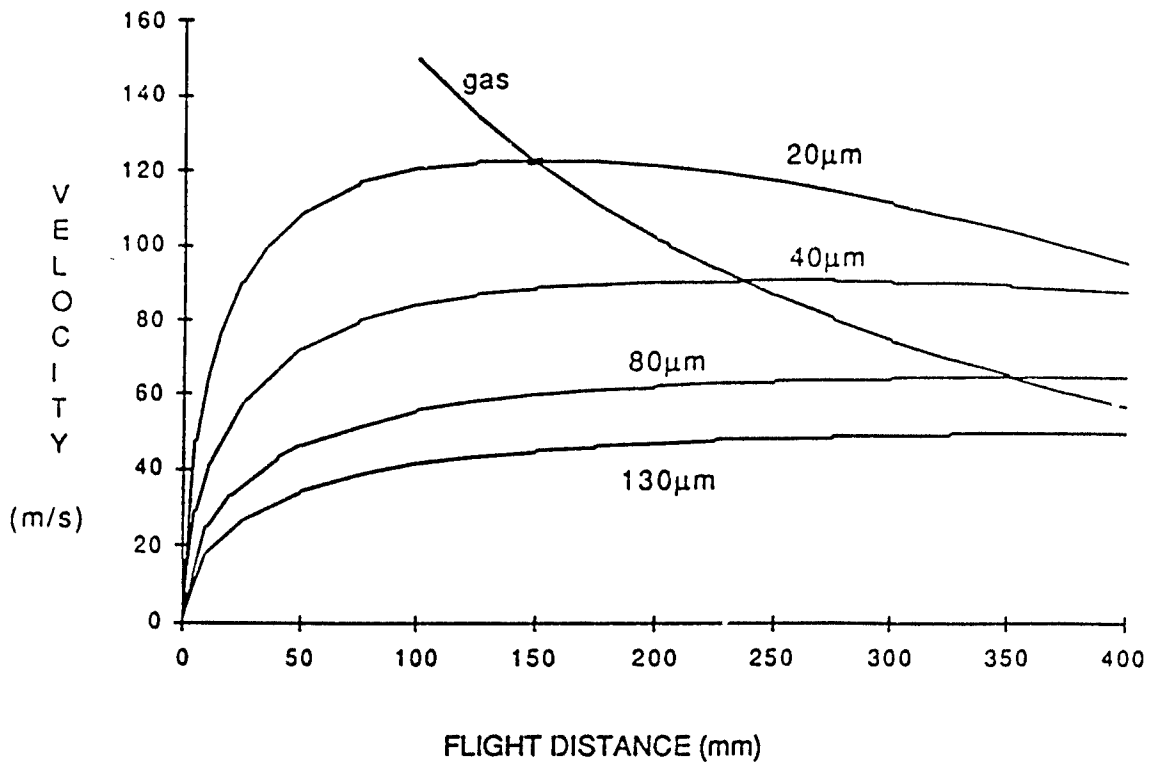


Fig. 5 Predicted variation of droplet velocity with flight distance for Ni-20 w/o Cr

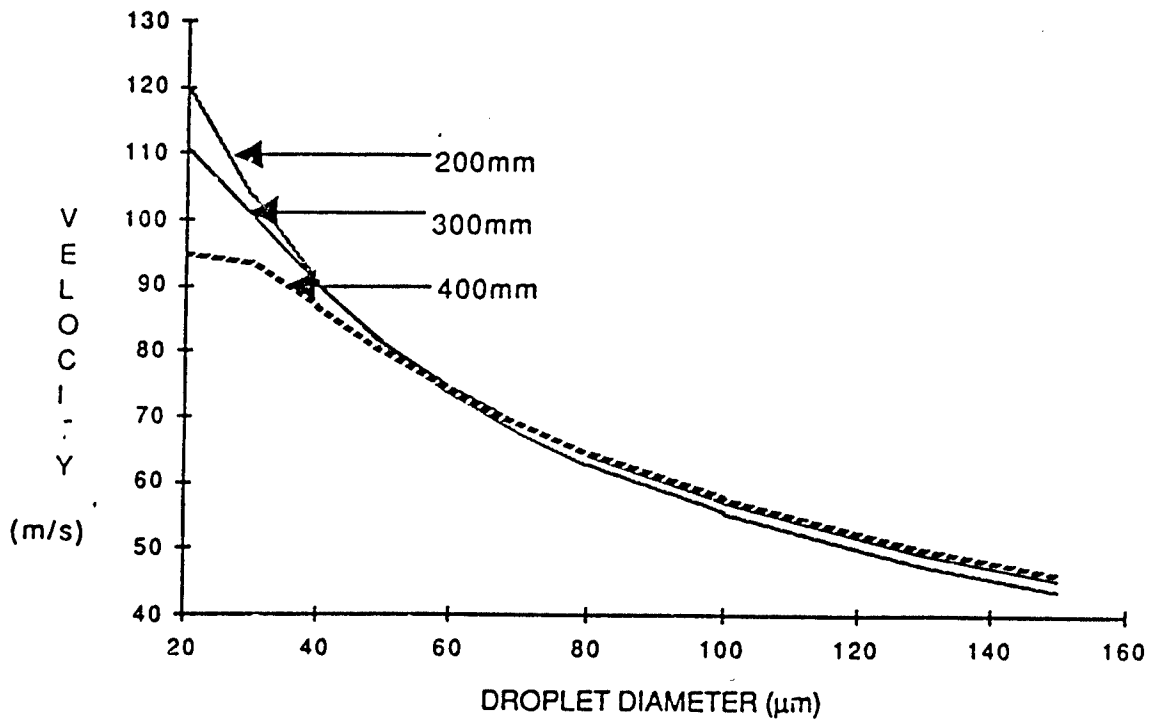


Fig. 6 Predicted droplet velocities as a function of droplet diameter and flight distance for Ni-20 w/o Cr

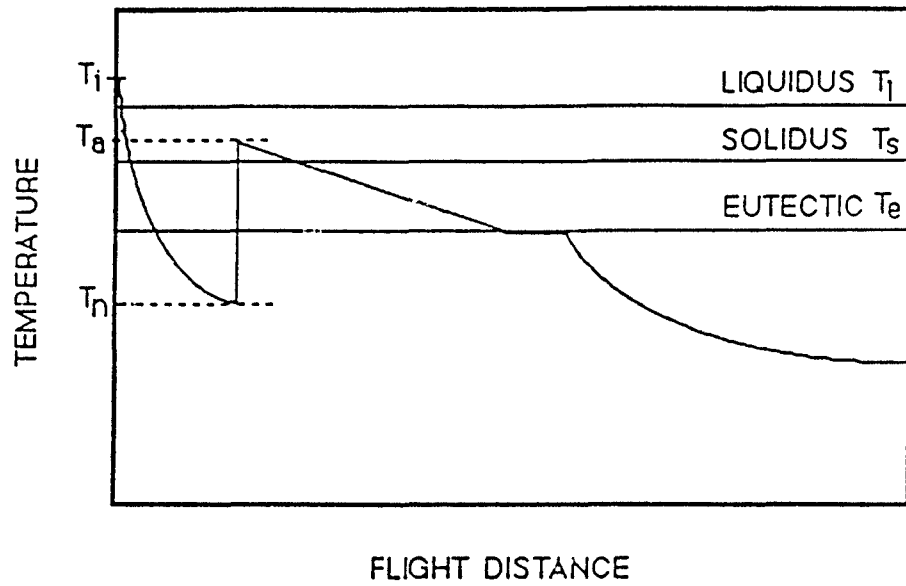


Fig. 7 Schematic of temperature profile of a droplet in flight

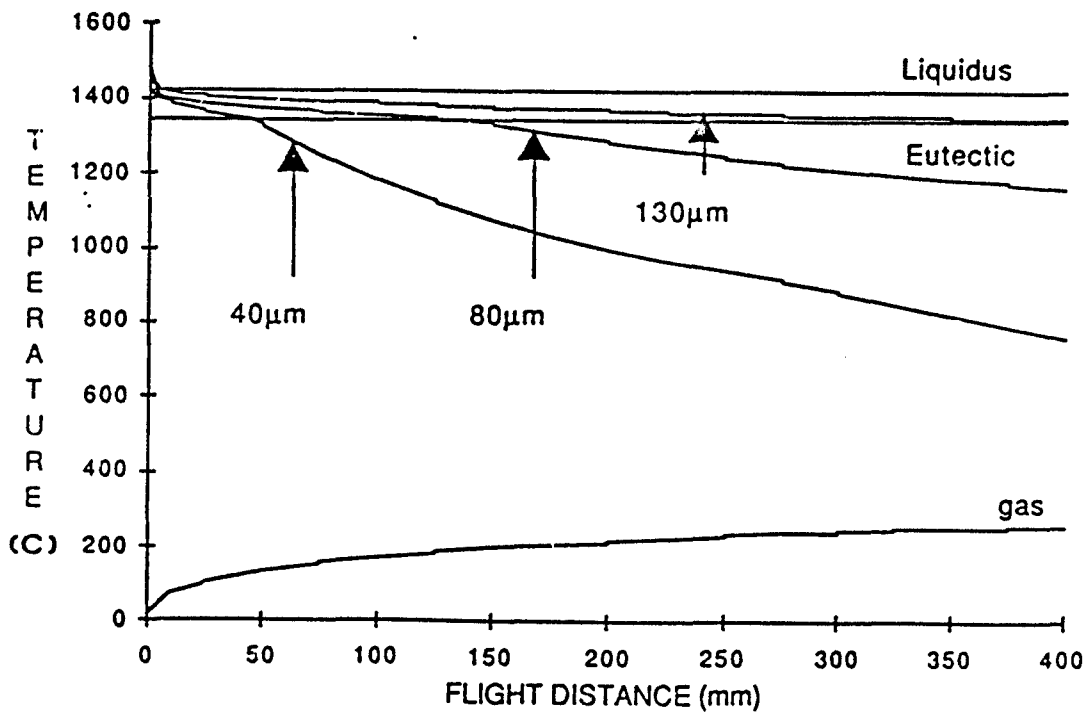


Fig. 8 Predicted variation of droplet temperature with flight distance for Ni-20 w/o Cr; no undercooling

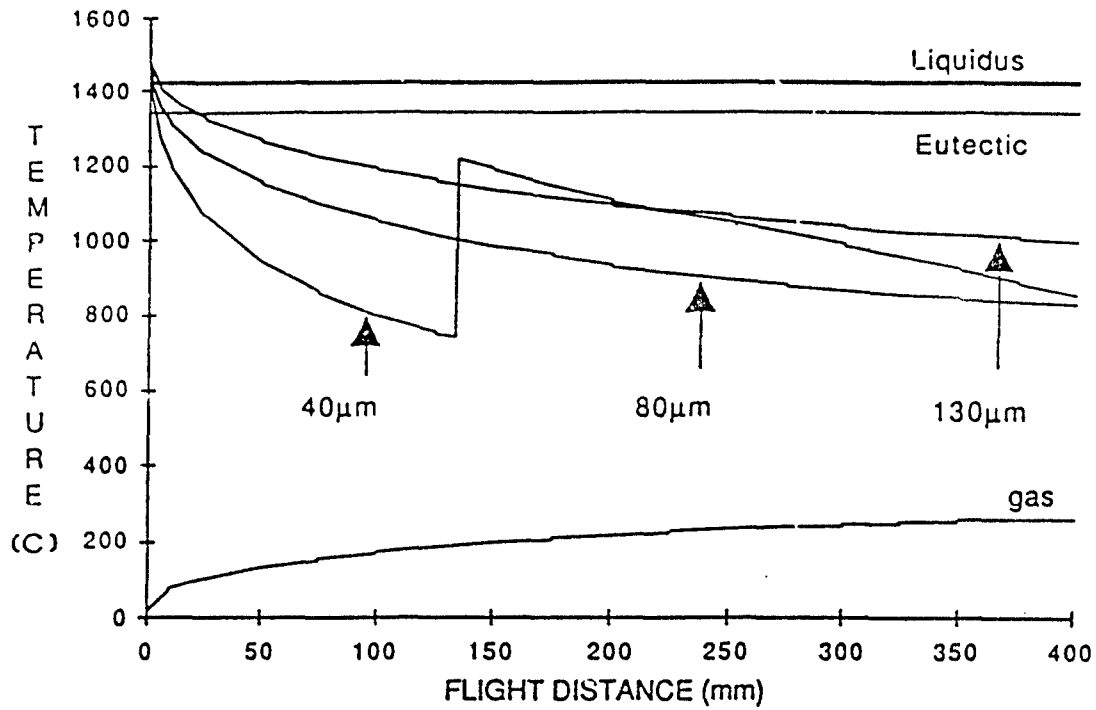


Fig. 9 Predicted variation of droplet temperature with flight distance for Ni-20 w/o Cr, homogeneous nucleation

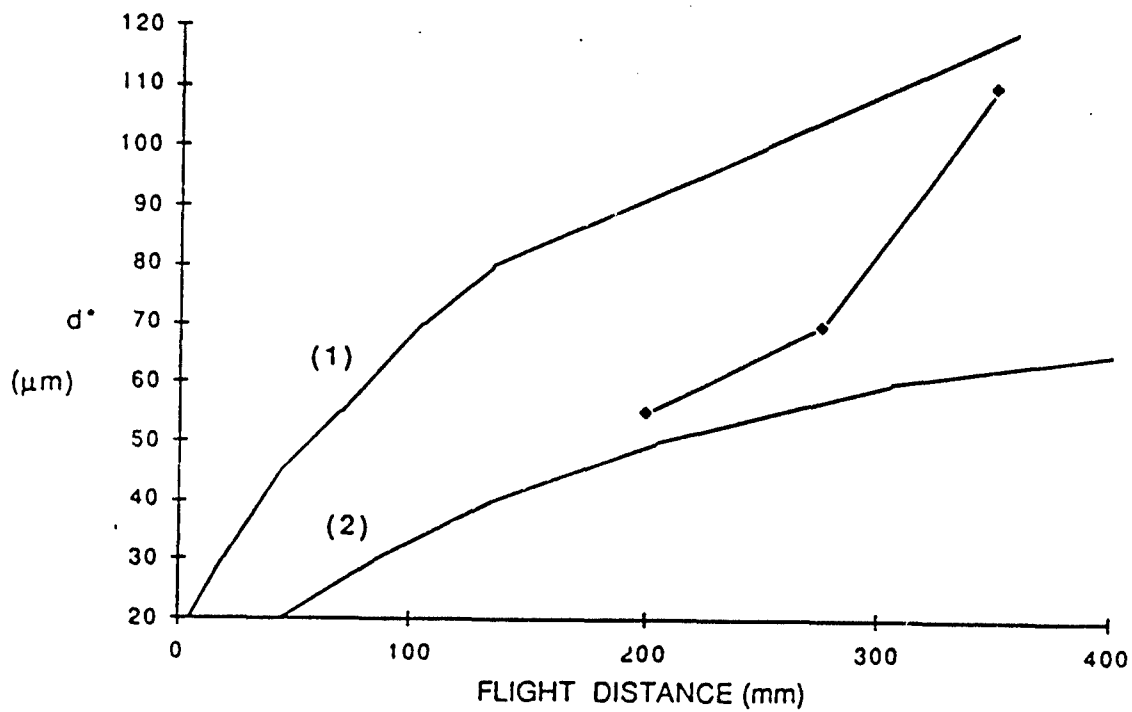


Fig. 10 Predicted variation of d^* with flight distance for Ni-20 w/o Cr. Curves (1) and (2) are for heterogeneous and homogeneous nucleation, respectively. Experimental data (◆) included for comparison

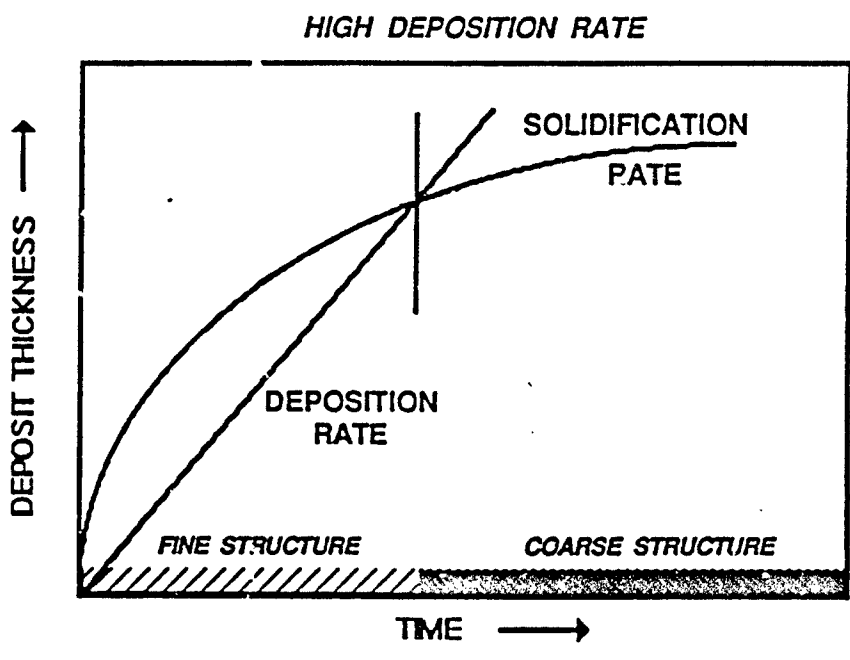
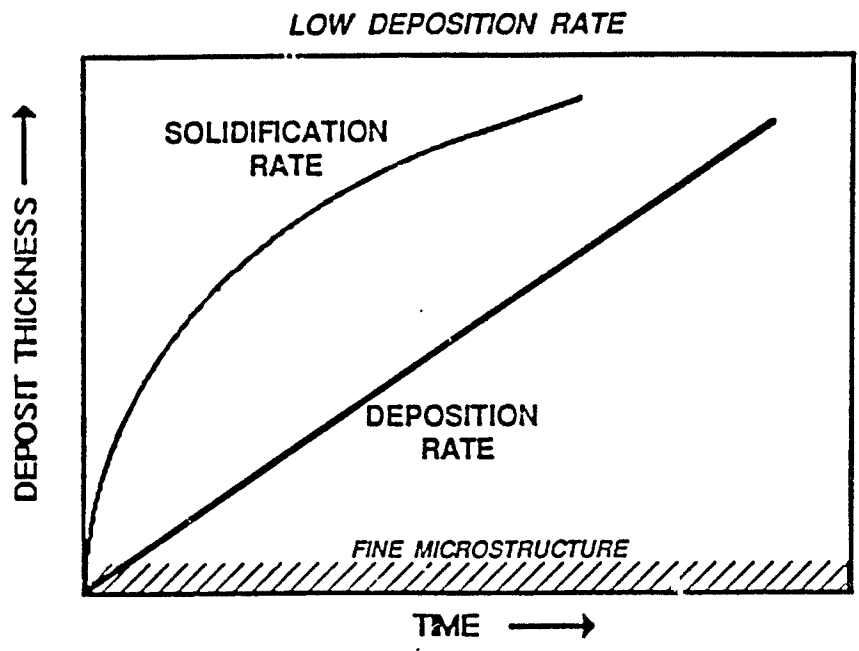


Fig. 11 Effect of deposition rate (D) and solidification rate (S) on microstructure in spray deposition

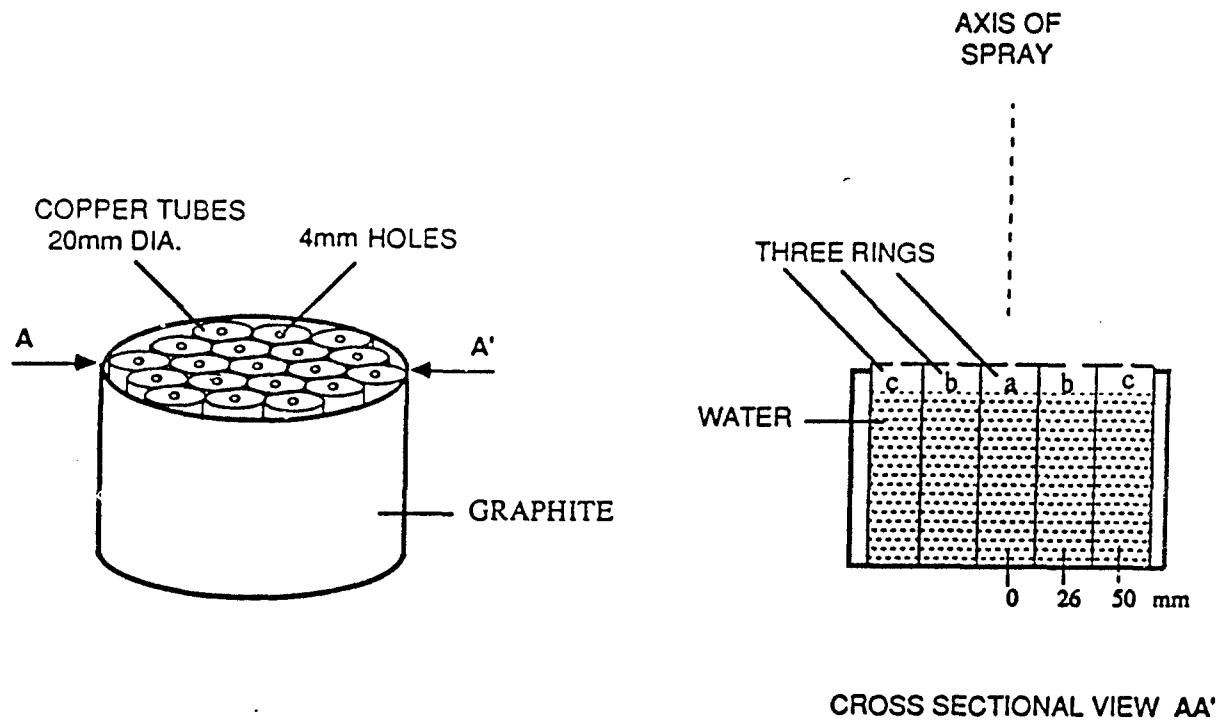


Fig. 12 Schematic of the set-up to collect droplets in three "rings" a, b and c

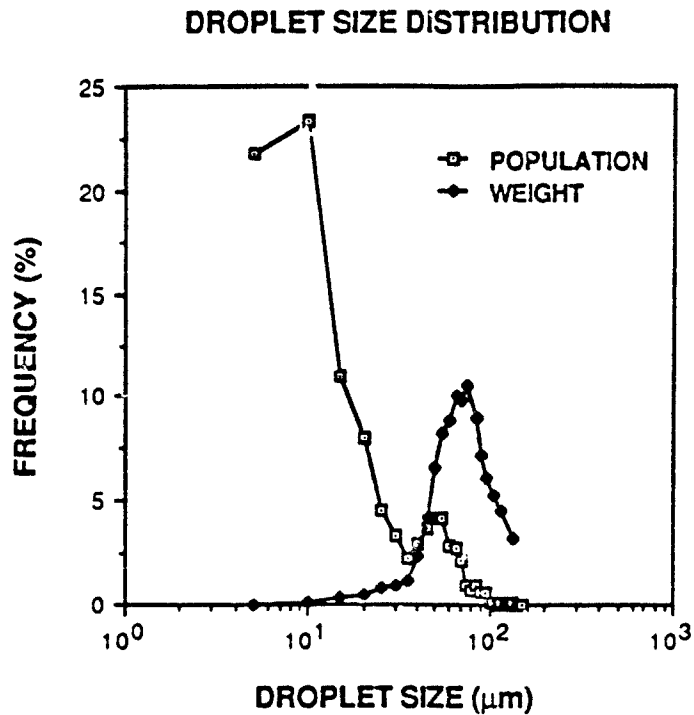


Fig. 13 Size distributions of Fe-20 w/o Mn droplets in the spray at a radial distance of 50mm; flight distance = 400mm

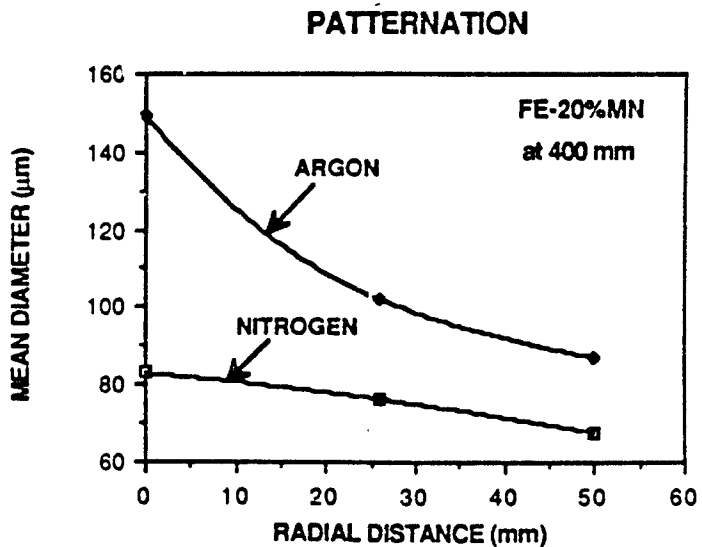


Fig. 14 Variation of mass-median droplet diameter with radial distance from the spray axis; flight distance = 400mm; Fe-20 w/o Cr

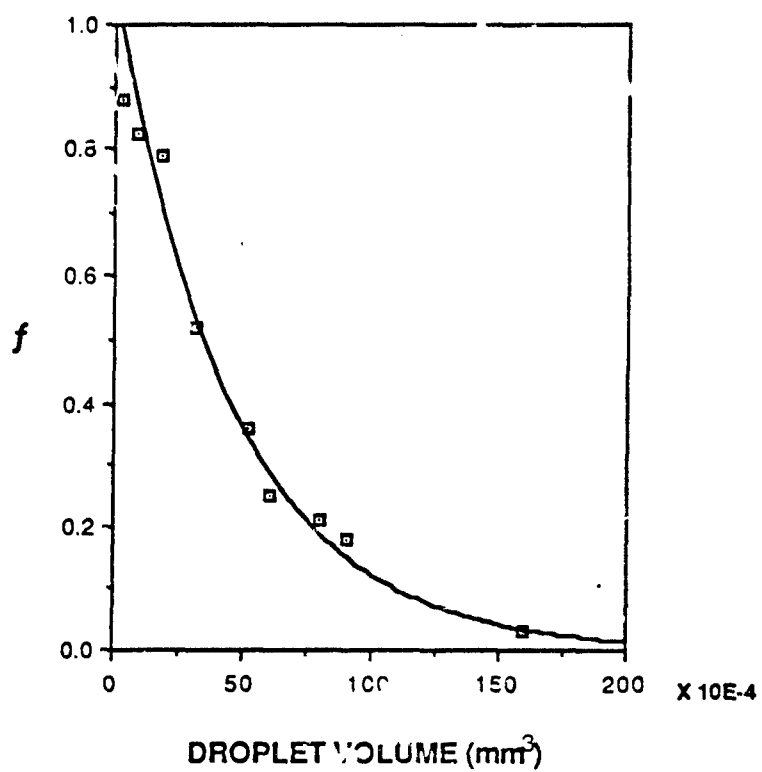
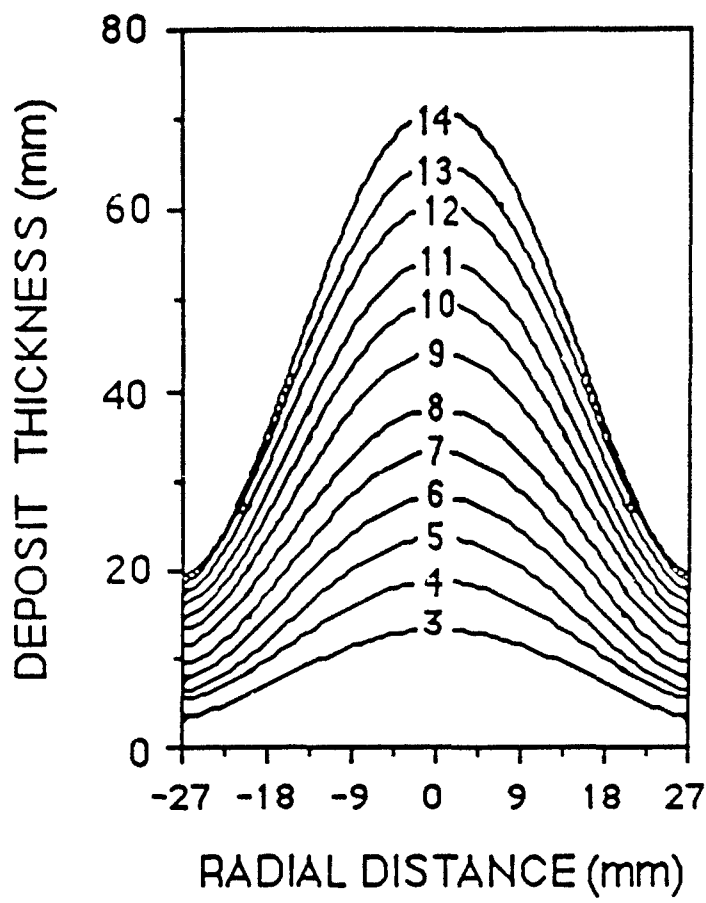
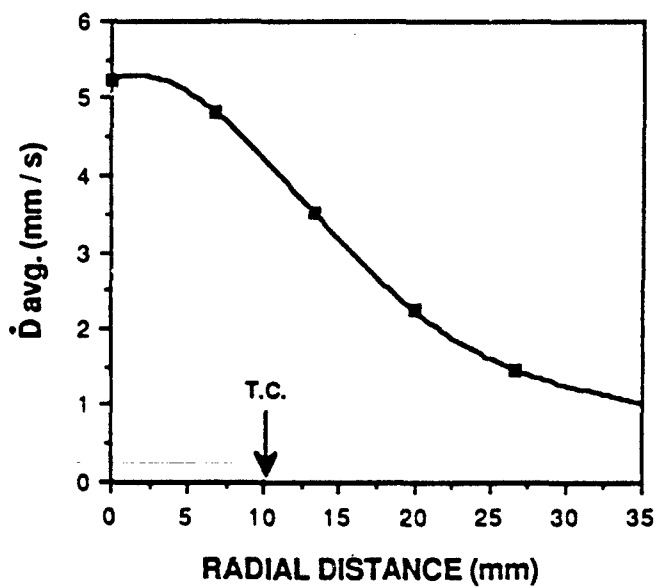


Fig. 15 Effect of droplet volume on the degree of undercooling of the droplets. f is the fraction of undercooling by homogeneous nucleation



(a)



(b)

Fig. 16 (a) Thickness profiles recorded during deposit build up on a stationary substrate, at different intervals (sec.) from the start of deposition
 (b) Dependence of the time averaged deposition rate on radial distance from the spray axis

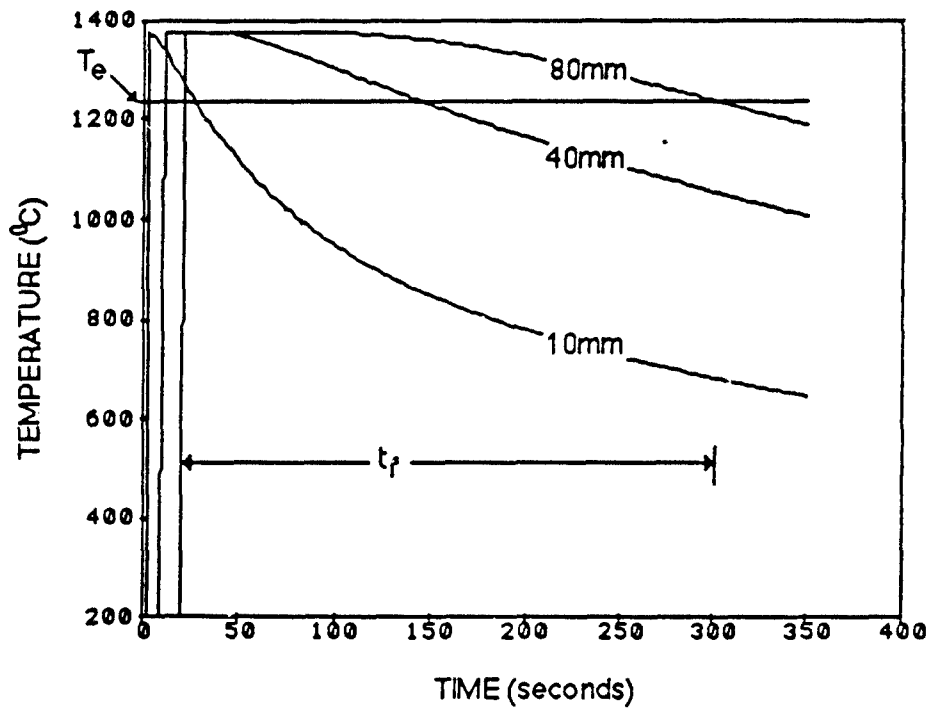
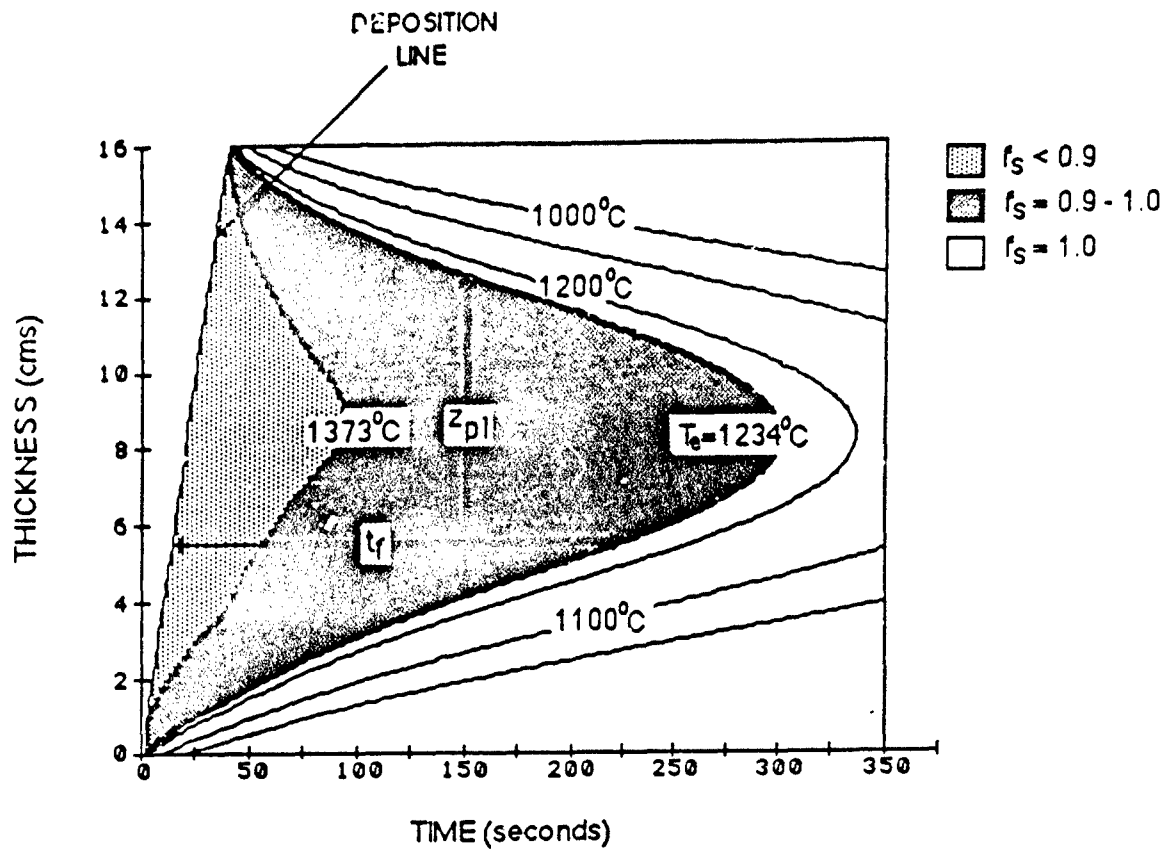


Fig. 17 (a) Predicted isotherms in a spray deposit as a function of time; Fe-20 w/o Cr, $\dot{D}=4\text{mm/s}$, $T_{\text{spray}}=1395^\circ\text{C}$, $h_s=h_g=10^3\text{ W/m}^2/\text{K}$.
 (b) Predicted dependence of temperature with time at three distances above the substrate; from (a)

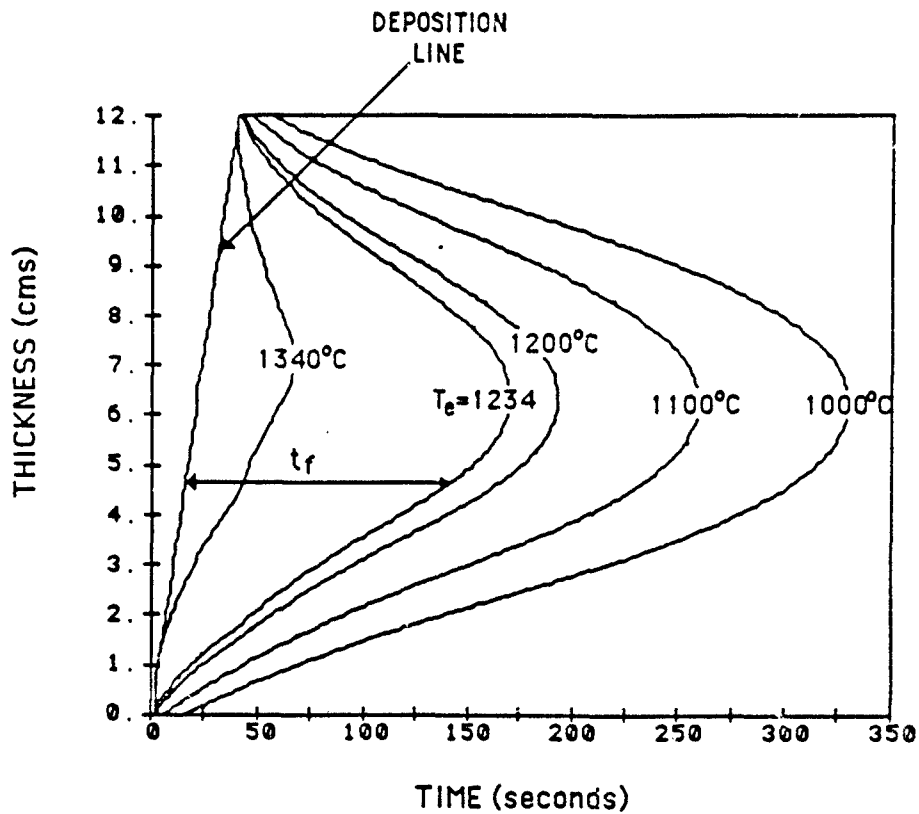


Fig. 18 Predicted isotherms in a spray deposit as a function of time;
 Fe-20 w/o Cr, $\dot{D}=3\text{mm/s}$, $T_{\text{spray}}=1395^\circ\text{C}$, $h_s=h_g=10^3\text{ W/m}^2/\text{K}$.

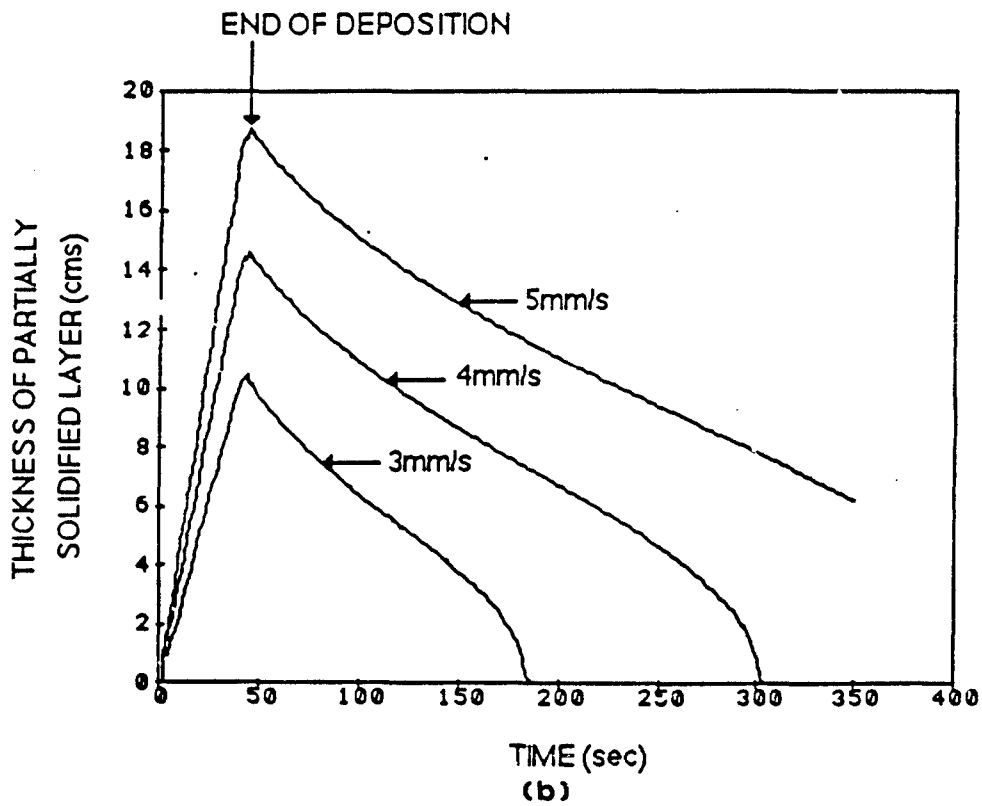
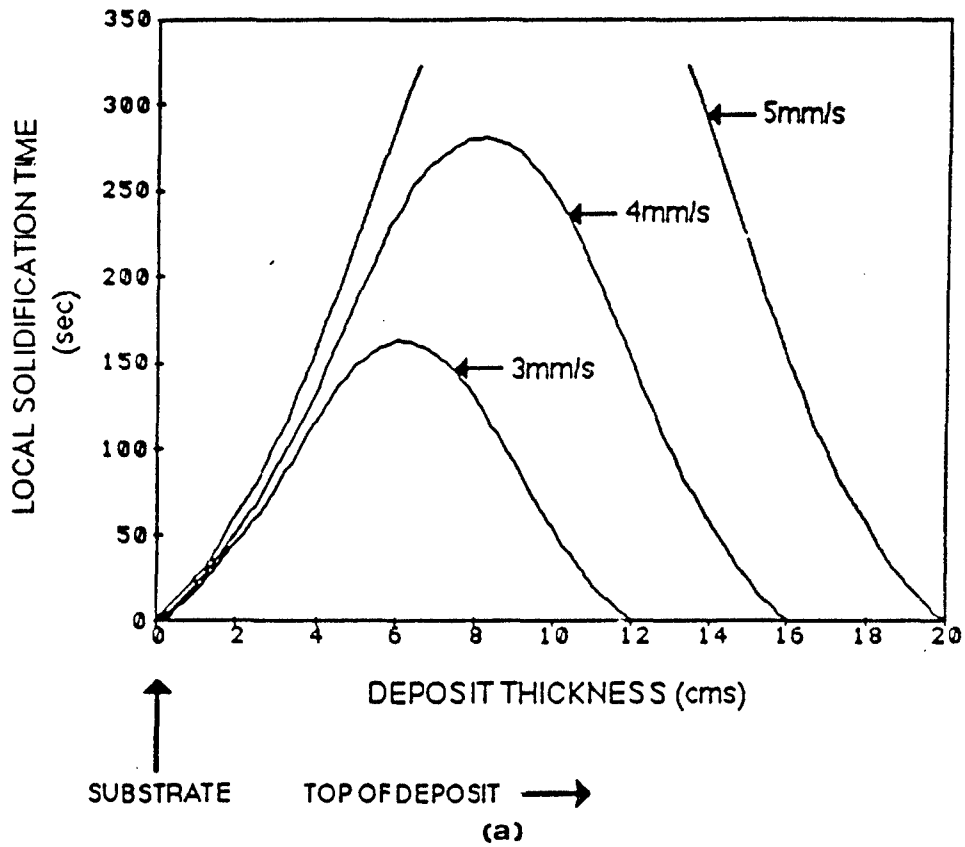


Fig. 19 (a) Predicted variation of local solidification time at different locations within the deposit and (b) thickness of partially liquid layer as a function of time; Fe-20 w/o Cr, $\dot{D}=4\text{mm/s}$, $T_{\text{spray}}=1395^{\circ}\text{C}$, $h_s=h_g=10^3\text{ W/m}^2/\text{K}$.

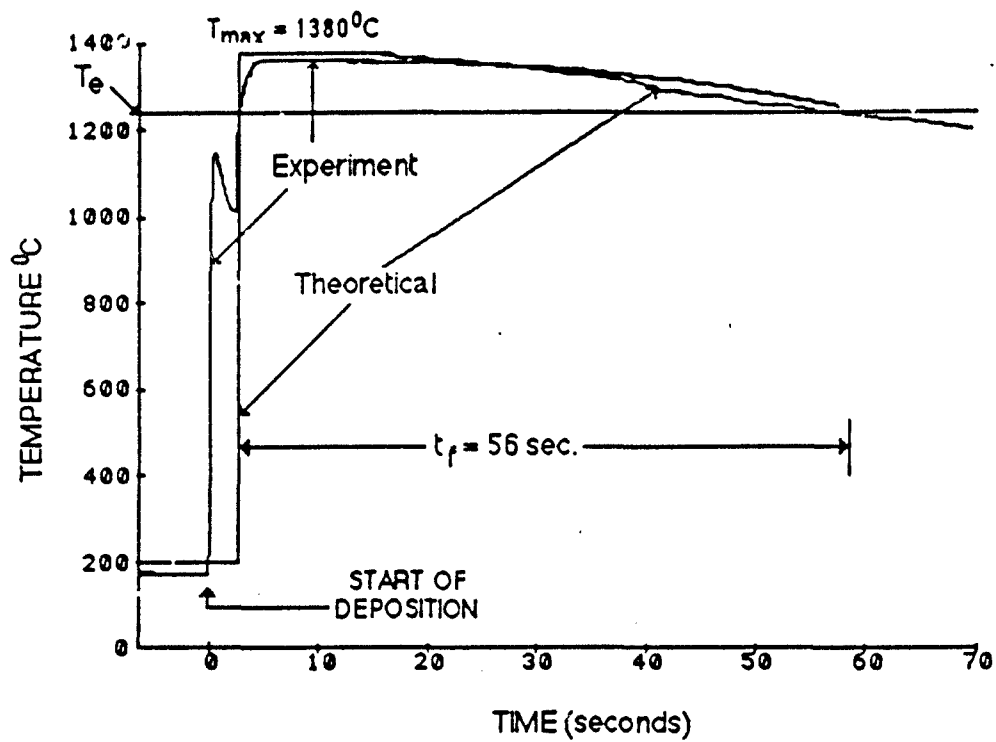


Fig. 20 Theoretical and experimental cooling curves in the spray deposit at a height of 20mm above the substrate; Fe-20 w/o Cr, $\dot{D}=4\text{mm/s}$

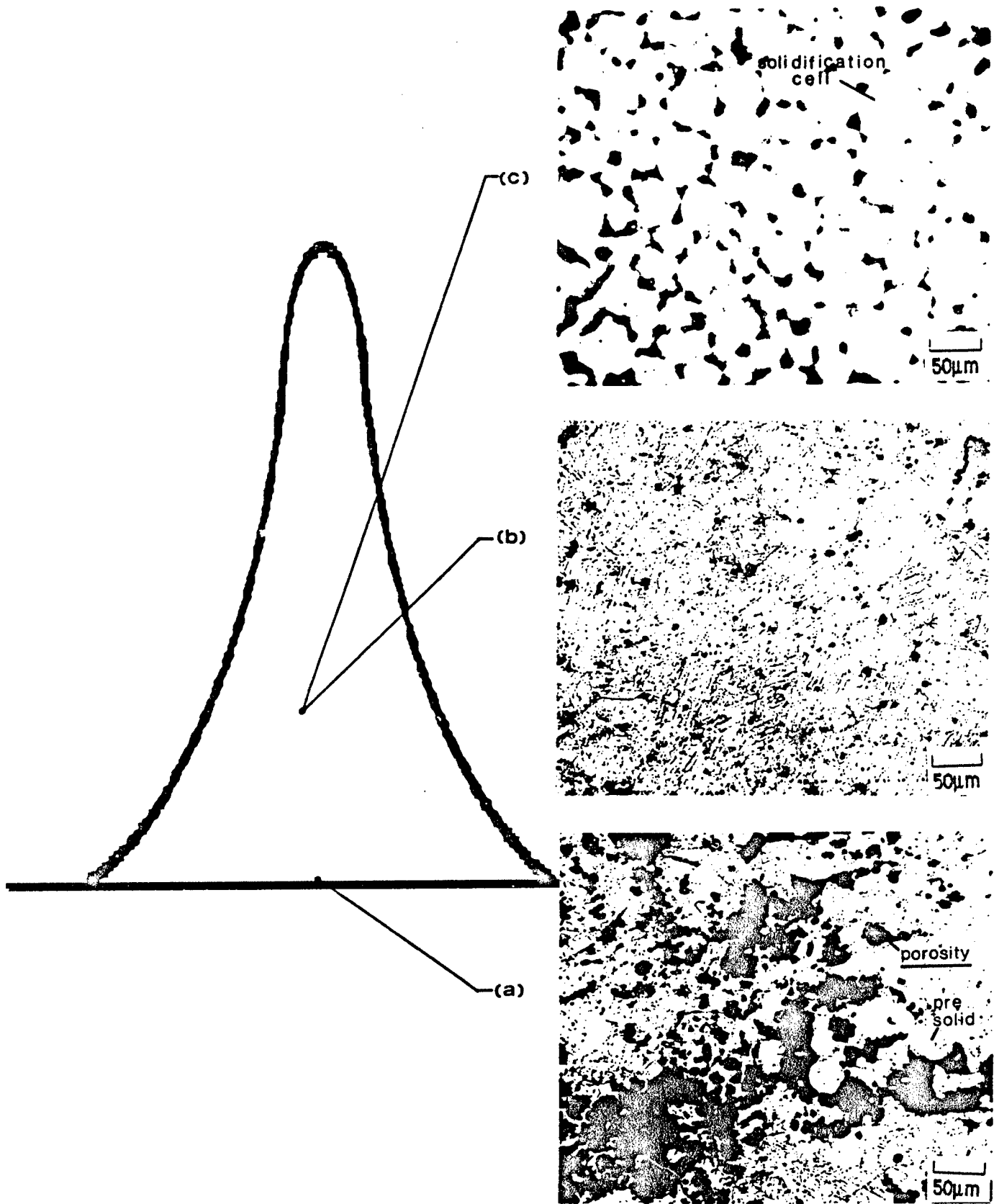


Fig. 21 Microstructure across a sprayed deposit of Fe-20 w/o Cr showing martensitic plates (in a and b) and solidification cells (in c)

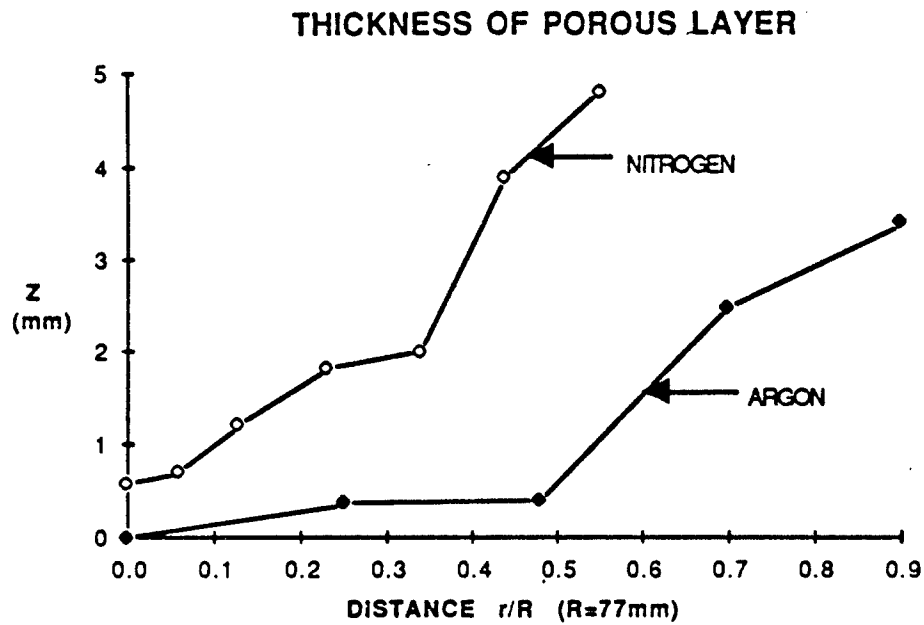


Fig. 22 Variation of the thickness of the initial porous layer in a Fe-20 w/o Cr deposit as a function of radial distance from the spray axis (i.e. \dot{D}). Data is presented for atomization with two different gasses, nitrogen and argon

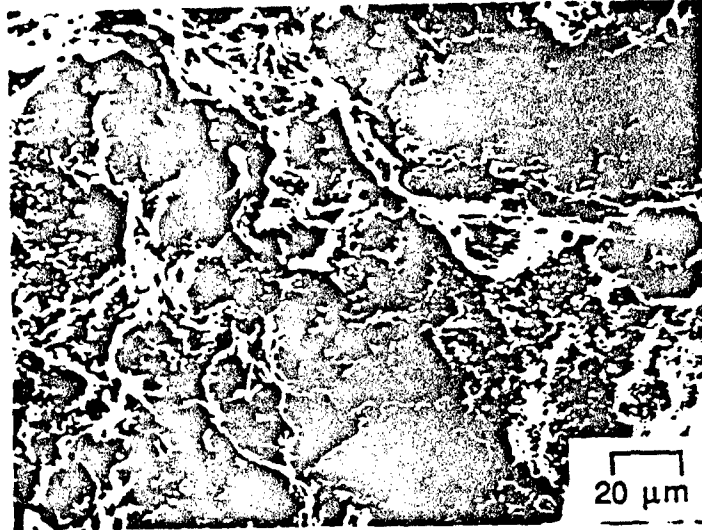


Fig. 23 SEM micrograph of a lightly polished and etched surface of Fe-20 w/o Cr deposit showing presolidified droplets and fragmented dendrite particles

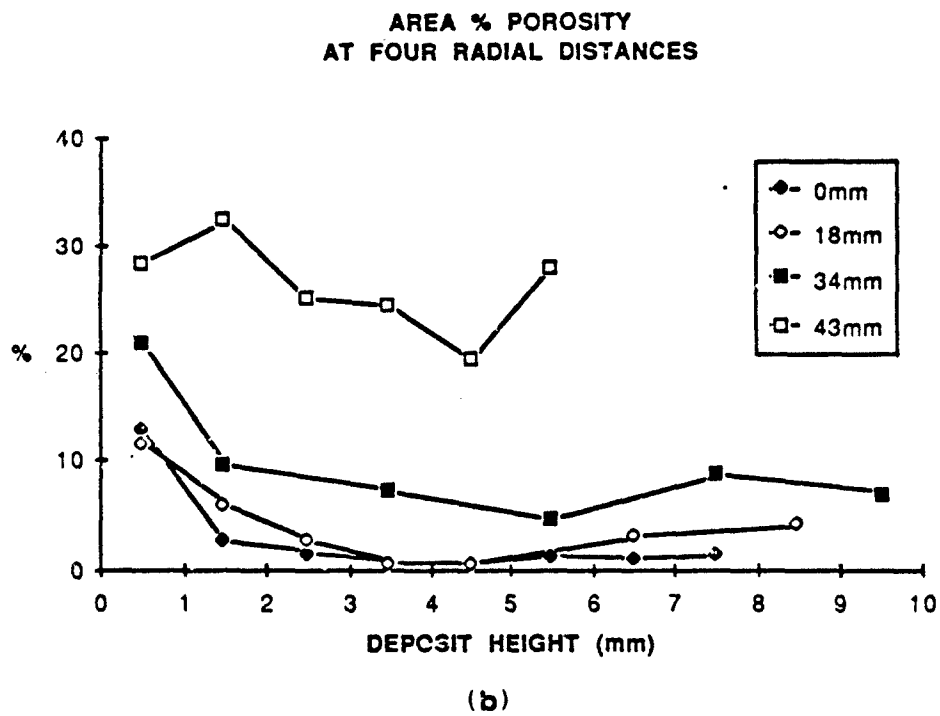
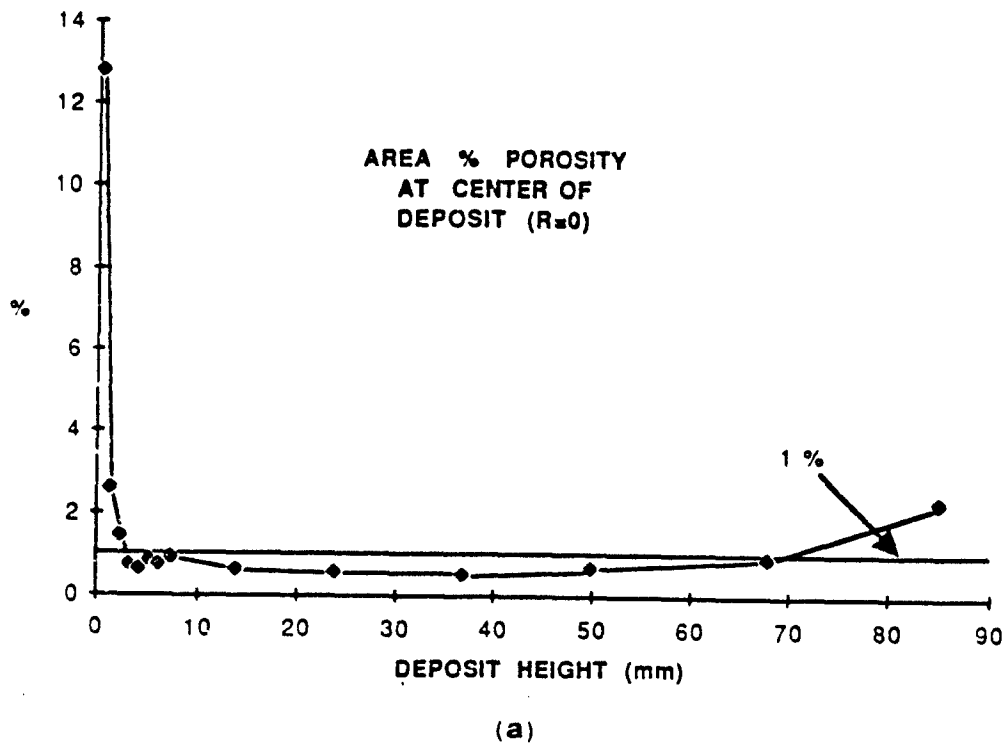


Fig. 24 (a) Percent porosity vs deposit thickness at the spray axis; total height of deposit = 90mm, Fe-20 w/o C
 (b) Measured variation of porosity as a function of deposit height at four radial distances from the spray axis (i.e. four values of \dot{D})

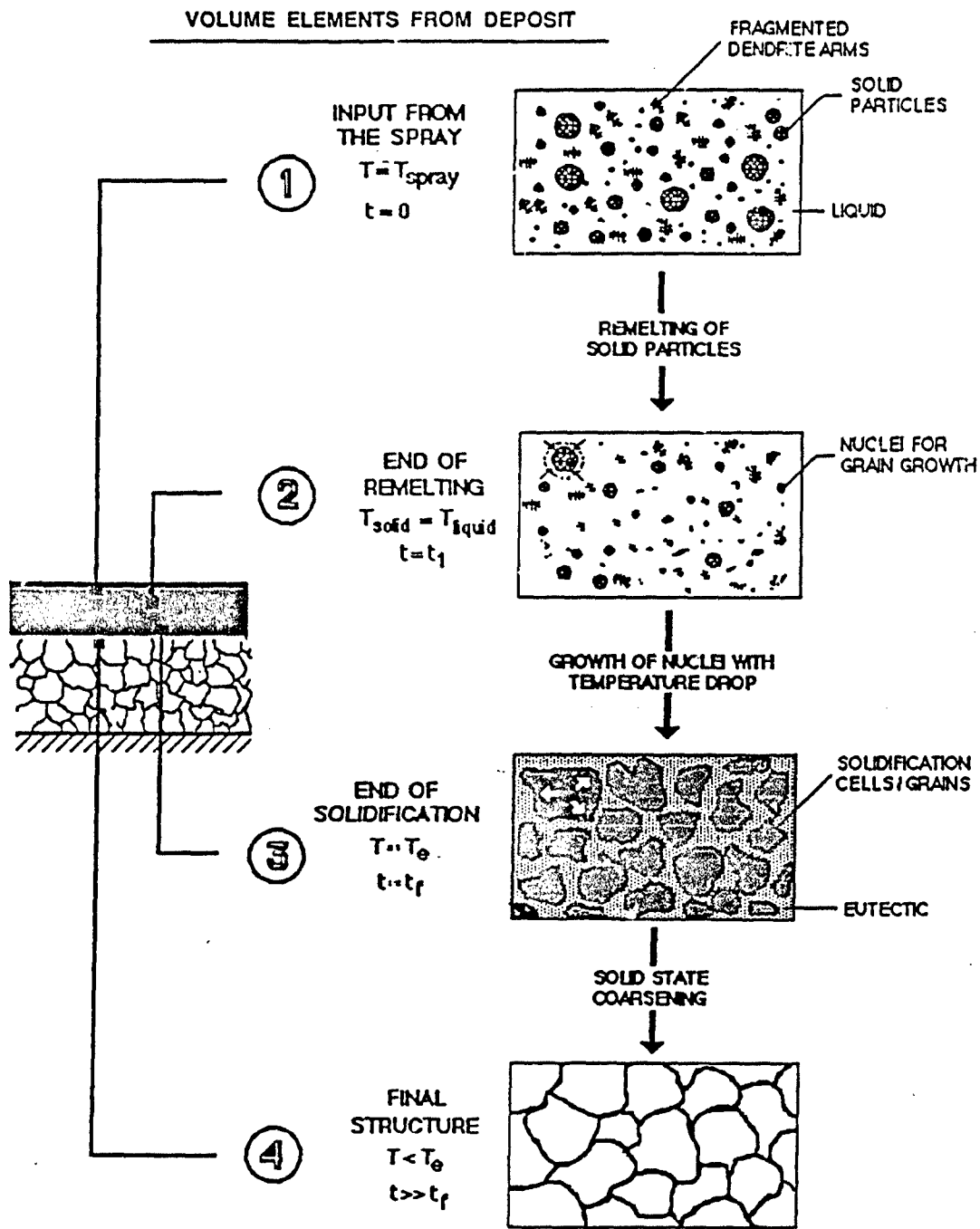


Fig. 25 Schematic of microstructural evolution within a volume element in the spray deposit

REPORT DOCUMENTATION PAGE		READ INSTRUCTIONS BEFORE COMPLETING FORM
1. REPORT NUMBER	2. GOVT ACCESSION NO.	3. RECIPIENT'S CATALOG NUMBER
4. TITLE (And Subtitle) SPRAY DEPOSITION: A FUNDAMENTAL STUDY OF DROPLET IMPINGEMENT, SPREADING AND CONSOLIDATION		5. TYPE OF REPORT & PERIOD COVERED 1 July 1986 - 30 June 1987
7. AUTHOR(s) D. Apelian, A. Lawley, G. Giilen and P. Mathur		6. PERFORMING ORG. REPORT NUMBER
9. PERFORMING ORGANIZATION NAME AND ADDRESS Department of Materials Engineering Drexel University Philadelphia, PA 19104		8. CONTRACT OR GRANT NUMBER(s) N 00014-84-K-0472; NR 650-025
11. CONTROLLING OFFICE NAME AND ADDRESS Office of Naval Research 800 N. Quincy Street Arlington, VA 22217		10. PROGRAM ELEMENT, PROJECT, TASK AREA & WORK UNIT NUMBERS
14. MONITORING AGENCY NAME & ADDRESS (if different from Controlling Office)		12. REPORT DATE September 1987
		13. NUMBER OF PAGES
		15. SECURITY CLASS. (of this report) Unclassified
		15a. DECLASSIFICATION DOWNGRADING SCHEDULE
16. DISTRIBUTION STATEMENT (of this Report) Approved for public release; distribution unlimited.		
17. DISTRIBUTION STATEMENT (of the abstract entered in Block 20, if different from Report)		
18. SUPPLEMENTARY NOTES		
19. KEY WORDS (Continue on reverse side if necessary and identify by block number) Spray Deposition, Osprey Process, Near Net Shape Manufacturing, Process Fundamentals, Mathematical Modeling, Droplet Velocity and Temperature, Deposit Heat Transfer, Solidification Rates, Microstructural Evolution		
20. ABSTRACT (Continue on reverse side if necessary and identify by block number) See over		

Net or near net shape products can be manufactured by technologies involving solidification processing, metal forming, particulate processing, and droplet consolidation. One example of droplet consolidation is spray deposition in the OspreyTM mode. In this process, a stream of liquid metal is atomized by an inert gas to form a spray of molten droplets; these are accelerated towards a substrate where they impinge and consolidate. Mathematical models have been developed to describe droplet-gas interactions in flight and droplet behavior on impact with the substrate. The models predict droplet velocity and temperature as a function of flight distance, the extent of droplet solidification on arrival at the substrate, and temperature distribution in the consolidated material during deposition. Measured values of droplet velocity, the progress of droplet solidification, and attendant temperature profiles after consolidation on the substrate substantiate the integrity of the models. This approach demonstrates the utility of modeling studies in order to establish quantitative guidelines for optimization of the process in terms of the evolution of microstructure in droplet consolidation.